

CZECH TECHNICAL UNIVERSITY IN
PRAGUE

Faculty of Nuclear Sciences and Physical
Engineering
Department of Physics



Research project

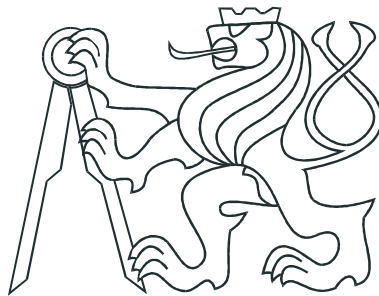
**Coherent photoproduction of J/ψ in Pb–Pb
collisions with emission of forward neutrons**

Vendulka Fílová

Supervisor: prof. Jesús Guillermo Contreras Nuño, Ph.D.

Prague, 2019

ČESKÉ VYSOKÉ UČENÍ TECHNICKÉ
V PRAZE
Fakulta Jaderná a Fyzikálně Inženýrská
Katedra Fyziky



Výzkumný úkol

**Koherentní fotoprodukce J/ψ v Pb–Pb
srážkách s emisí dopředných neutrnů**

Vendulka Fílová

Vedoucí: prof. Jesús Guillermo Contreras Nuño, Ph.D.

Praha, 2019



Katedra: fyziky

Akademický rok:

2018/2019

VÝZKUMNÝ ÚKOL

Student: Bc. Vendulka Fílová

Studijní program: Aplikace přírodních věd

Obor: Experimentální jaderná a částicová fyzika

Vedoucí úkolu: doc. Jesús Guillermo Contreras Nuño, Ph.D.

Název úkolu (česky/anglicky):

Koherentní J/ψ fotoprodukce v Pb-Pb srážkách s emisí dopředných neutronů

Coherent J/ψ photoproduction in Pb-Pb collisions with forward neutrons

Pokyny pro vypracování:

- 1) Vypracovat rešerši na téma:
 - a. Měření koherentní J/ψ fotoprodukce v AA srážkách na CMS a ALICE.
 - b. Model koherentní produkce s emisí neutronů.
- 2) Studium koherentní J/ψ fotoprodukce v dopředné rapiditě v Pb-Pb srážkách z ALICE dat z LHC run 2 s emisí dopředných neutronů.

Výzkumný úkol bude vypracován v anglickém jazyce.

Součástí zadání výzkumného úkolu je jeho uložení na webové stránky katedry fyziky.

Literatura:

- [1] J. G. Contreras, J.D. Tapia Takaki, Ultra-peripheral heavy-ion collisions at the LHC. International Journal of Modern Physics A 30(8), s. 1542012 (2015)
- [2] V. Khachatryan et al., Coherent J/ψ photoproduction in ultra-peripheral PbPb collisions at $\sqrt{s_{NN}} = 2.76$ TeV with the CMS experiment. Physics Letters B 772, s. 489–511 (2017)
- [3] B. Abelev et al., Coherent J/ψ photoproduction in ultra-peripheral Pb-Pb collisions at $\sqrt{s_{NN}} = 2.76$ TeV. Physics Letters B 718, s. 1273 – 1283 (2012)
- [4] V. Guzey, E. Kryshen, M. Zhalov, Coherent photoproduction of vector mesons in ultraperipheral heavy ion collisions: Update for run 2 at the CERN Large Hadron Collider. Phys. Rev. C 93, 055206 (2016)

Datum zadání: 22. 10. 2018

.....

Datum odevzdání: 30. 06. 2019

vedoucí katedry

Prohlášení:

Prohlašuji, že jsem svůj výzkumný úkol vypracovala samostatně a použila jsem pouze podklady (literaturu, projekty, software, atd.) uvedené v příloženém seznamu.

Nemám závažný důvod proti užití tohoto školního díla ve smyslu § 60 Zákona č. 121/2000 Sb., o právu autorském, o právech souvisejících s právem autorským a o změně některých zákonů (autorský zákon).

V Praze dne

Vendulka Fílová

Acknowledgement

I would like to express my deep gratitude to my supervisor, prof. Jesús Guillermo Contreras Nuño, Ph.D. Without his patience, encouragement and constant help both with physics and programming this thesis would not have been possible. My thanks also goes to Mgr. Michal Broz, Ph.D. who provided the used data sets. A special thanks goes to my family, especially to my partner Honza for his patience and great support during the realization of this work.

Title:

Coherent photoproduction of J/ψ in Pb–Pb ultra-peripheral collisions with emission of forward neutrons

Author: Vendulka Fílová

Branch of study: Experimental Nuclear and Particle Physics

Sort of project: Research project

Supervisor: prof. Jesús Guillermo Contreras Nuño, Ph.D., Department of Physics, Faculty of Nuclear Sciences and Physical Engineering, Czech Technical University in Prague

Abstract:

The nuclear gluon distribution is not equal to sum of the gluon distributions of nucleons inside the nucleus. This phenomenon is called the gluon nuclear shadowing and it becomes effective in the small- x region. This phenomenon is not well understood and it is a current topic of interest. Measuring the cross section of coherent photoproduction of a J/ψ meson in ultra-peripheral collisions is a tool for investigating the gluon structure of proton, nucleus and nuclear shadowing at low- x . Studying photoproduction of J/ψ accompanied by additional forward neutron emission gives us the opportunity to reach even lower values of x .

Key words: Nuclear shadowing, J/ψ meson, ultra-peripheral heavy-ion collisions, exclusive photoproduction

Název práce:

Koherentní fotoprodukce J/ψ v ultra-periferálních Pb–Pb srážkách s emisí dopředných neutronů

Autor: Vendulka Fílová

Abstrakt:

Distribuce gluonů v jádře není stejná jako součet gluonových distribucí nukleonů nacházejících se v jádře. Tento jev nazýváme jaderné stínění a je pozorován pro malá Bjorkenova x . Tento jev není zatím dobře objasněn a je tématem dnešního zájmu. Měřením účinného průřezu koherentní fotoprodukce vektorového mezonu J/ψ v ultra-periferálních srážkách můžeme zkoumat gluonovou strukturou nukleonů, jader a jaderné stínění pro nízké hodnoty x . Studium koherentní fotoprodukce s emisí dopředných neutronů nám otevírá možnost dosáhnout dokonce ještě nižších hodnot x .

Klíčová slova: Jaderné stínění, J/ψ mezon, ultra–periferální těžko-iontové srážky, exkluzivní fotoprodukce

Contents

1	Introduction	1
2	Structure of nucleon	3
2.1	First experiments	3
2.2	Feynman's parton model	6
2.3	Saturation	7
2.4	Nuclear shadowing	7
3	Exclusive coherent photoproduction of a J/ψ in ultra-peripheral collisions	10
3.1	Ultra-peripheral collisions	10
3.2	Exclusive photonuclear process	10
3.3	Cross section	12
3.4	Exclusive photoproduction of charmonia on nuclei in LO perturbative QCD	14
4	ALICE detector	17
4.1	Inner Tracking System (ITS)	17
4.2	Muon Spectrometer	19
4.2.1	Absorbers	20
4.2.2	Dipole magnet	20
4.2.3	The Tracking System	21
4.2.4	Trigger system	21
4.3	The Zero Degree Calorimeters (ZDCs)	22
4.4	ALICE Diffractive Detector (AD)	23
4.5	VZERO detector	24
5	Previous measurements	27
5.1	Coherent J/ψ photoproduction in ultra-peripheral Pb–Pb collisions at $\sqrt{s_{NN}} = 2.76\text{TeV}$ [1]	27
5.1.1	Data selection	27
5.1.2	Results	28
5.2	Coherent J/ψ photoproduction at forward rapidity in ultra-peripheral Pb–Pb collisions at $\sqrt{s_{NN}} = 5.02\text{ TeV}$ [2]	30
5.2.1	Results	31
5.3	Coherent J/ψ photoproduction on ultra-peripheral Pb–Pb collisions at $\sqrt{s_{NN}} = 2.76$ with the CMS experiment [3]	35
5.3.1	Data selection	35
5.3.2	Results	37

6	Analysis	44
6.1	Data samples	44
6.2	The triggers	45
6.3	Selection of events	46
6.3.1	Event selection criteria	46
6.3.2	Track selection	46
6.3.3	Dimuon selection	46
6.4	The invariant mass distribution	47
6.5	Energy spectrum of ZDC	47
6.6	Transverse momentum distribution	49
6.7	Rapidity distribution	49
7	Summary	54

List of Figures

1.1	Feynman diagram for the photoproduction of a J/ψ vector meson with the emission of forward neutron.	2
2.1	The measured differential cross section in comparison with theoretical calculations [4].	4
2.2	Deep inelastic scattering of an electron on a proton, in the Bjorken frame where the proton has very large energy while the virtual photon γ^* has small longitudinal momentum. In the Bjorken frame, also called the infinite momentum frame, the mass of the proton can be ignored as well as the mass of its constituents, the valence quarks.	5
2.3	The parton momentum distributions f_i describe the probability that the struck parton i carries a fraction x of proton's momentum P [5].	6
2.4	The parton distribution functions of a proton in dependence on x , measured at HERA [6].	8
2.5	Schematic behavior of the ratio $R_{F_2}^A(x, Q^2)$ in dependence on x for a fixed Q^2 [7].	9
3.1	Schematic illustration of an ultra-peripheral collision of two nuclei, two contracted pancakes. The impact parameter of the collision b is larger than the sum of the two radii, R_A and R_B [8].	11
3.2	Different types of reactions possible in UPCs, (a)-photon-photon collision, (b)-photonuclear collision and (c)-photonuclear reaction with nuclear breakup due to additional photon exchange [8].	12
3.3	The $d\sigma_{PbPb \rightarrow J/\psi PbPb}(y)/dy$ cross section as a function of the J/ψ rapidity y at $\sqrt{s_{NN}} = 5.02$ TeV predicted by LO pQCD in Eq. 3.7 and Eq. 3.8 with the gluon shadowing ratio $R_g(x, \mu^2)$ of the leading twist nuclear shadowing model. The shaded areas span the range of predictions corresponding to the upper and lower limits on $R_g(x, \mu^2)$. The left upper plot shows the total cross section, the other plots show different neutron emission channels. Figure taken from [9].	15
3.4	The prediction of $d\sigma_{PbPb \rightarrow J/\psi PbPb}(y)/dy$ cross section as a function of the J/ψ rapidity y at $\sqrt{s_{NN}} = 5.02$ TeV of LO pQCD with the EPS09 gluon shadowing ratio $R_g(x, \mu^2)$. The shaded areas show the uncertainties of $R_g(x, \mu^2)$. The dashed curves labeled "one-side" show the contribution of the first term in Eq. 3.1. Figure taken from [9]	16
4.1	Schema of the ALICE detector with important subdetectors for this work highlighted [10].	18
4.2	The layout of the Inner Tracking System [11].	18

4.3	Transverse impact parameter resolution in dependence on p_T [11]. . .	19
4.4	Acceptance of the Muon Spectrometer as a function of p_T of J/ψ and $\Upsilon(1S)$ in the muon spectrometer rapidity range in their dimuon decay channel with a muon low p_T cut equal to 1 GeV [12].	20
4.5	The layout of the Muon Spectrometer. Stations 1-5 stands for the tracking system and stations 6-7 show the trigger system [12].	21
4.6	Layout of the front absorber of the Muon Spectrometer. Different materials which are used for the absorber are presented [13].	22
4.7	The cathode plane layout of Station 1 of the Tracking System of the Muon Spectrometer. Larger pads are used with larger distance from the beam line [13].	23
4.8	Layout of Tracking System Stations 4 and 5 which are located after the dipole magnet of the Muon Spectrometer [13].	24
4.9	A photograph of the Zero Degree Neutron Calorimeter [14].	25
4.10	The energy resolution of Zero Degree Calorimeter measured for hadron and electron beams. It is measured in dependence on $1/\sqrt{E}(\text{GeV})$ [14].	26
4.11	The final prototype of the ALICE Diffractive detector [10].	26
5.1	Invariant mass distribution for events with two oppositely charged muons in the rapidity range $-3.6 < y < -2.6$ [1].	29
5.2	Dimuon p_T distribution. The data is fitted summing four different Monte Carlo templates [1].	30
5.3	The differential cross section of coherently produced J/ψ at rapidity interval $-3.6 < y < -2.6$ which is shown by the vertical bar of the measurement point. The error is quadratic sum of the statistical and systematic errors. With the colored curves different theoretical predictions are shown [1].	31
5.4	The cross section integrated over the rapidity range $-3.6 < y < -2.6$ compared to the theoretical models [1].	32
5.5	Invariant mass distribution for muon pairs. The pink and red lines correspond to Crystall Ball functions representing J/ψ and ψ' signals. The dashed green line corresponds to the background and the solid blue line corresponds to the sum of background and signal functions [2].	33
5.6	Transverse momentum distribution for muon pairs in range $2.85 < m_{\mu\mu} < 3.35\text{GeV}/c^2$ [2].	34
5.7	The p_T distributions for different rapidity intervals for dimuons in the range $2.85 < m_{\mu\mu} < 3.35\text{GeV}/c^2$ [2].	39
5.8	Measured coherent differential cross section of photoproduced J/ψ in ultra-peripheral collisions at $\sqrt{s_{NN}} = 5.02$ TeV. The statistical uncertainties are represented by the error bars and the boxes around the points are the systematic errors. The colored lines represent different theoretical calculations and the green band represents the uncertainties of the EPS09 LO model discussed in Chapter 3 [2].	40
5.9	The dimuon invariant mass distribution for selected data in the range $2.6 < m(\mu^+\mu^-) < 3.5$ GeV for the break-up mode (Xn0n). The green curve is a second-order polynomial and represents the $\gamma + \gamma$ component and the black curve shows the sum of all components ($\gamma + \gamma$, coherent and incoherent J/ψ) [3].	41

5.10	The p_T distribution for opposite-sign muon pair with $p_T < 1.0\text{GeV}$ and $1.8 < y < 2.3$. The red, blue and green curves represent coherent, incoherent and $\gamma + \gamma$ events separately and the black line shows the sum of all components [3].	42
5.11	Differential cross section in dependence on rapidity for coherently photoproduced J/ψ measured by CMS and ALICE. The horizontal bars represent the rapidity range of the measurements and the vertical error bars include statistical and systematic uncertainties [3].	43
6.1	The mass spectrum of dimuon pair for different rapidity intervals. . .	50
6.2	Model of energy distribution (arb. unit) in neutron ZDC in UPC Pb–Pb collisions at $\sqrt{s_{NN}} = 5.02\text{ TeV}$ [15].	51
6.3	Timing information of ZNA and ZNC detectors within the range $-2.0 < t < 2.0\text{ ns}$ for 2015 data.	51
6.4	ZNA and ZNC energy spectrum for events within $-2.0 < t < 2.0\text{ ns}$ timing. The peaks correspond to neutron emission of $1n, 2n, 3n, 4n$. . .	52
6.5	ZNA (a) and ZNC (b) energy spectrum for events within $-2.0 < t < 2.0\text{ ns}$ timing. The peaks correspond to neutron emission of $1n, 2n, \dots$ and are fitted by the Gaussian. Data period 2018q.	52
6.6	The transverse momentum distribution for events which satisfy ZDC selection for different neutron channels, run period 2018r.	53
6.7	The transverse momentum distribution for events which satisfy ZDC selection for different neutron channels, run period 2018r.	53

Chapter 1

Introduction

An important phenomenon nowadays in the field of perturbative quantum chromodynamics (pQCD) is nuclear gluon shadowing. The shadowing refers to the behavior of the gluon distribution in a nucleon which is bounded inside the nucleus and the gluon distribution in a free nucleon. In the case of shadowing, the gluon distribution in the nucleus is suppressed with respect to that of gluon in a free nucleon.

According to pQCD, the nucleon is composed of valance quarks, sea quarks and gluons with different distributions. These distributions are called parton distribution functions (PDFs). The PDFs depend on the variable x which is the fractional momentum of a given parton in the nucleon; $x = p_{\text{parton}}/p_{\text{proton}}$. The PDFs have been widely studied and measured in dependence on x [16]. In the small- x region the gluon distribution function dominates and increasing as a power law for decreasing x . The gluon PDF raises so fast that at some point the unitarity of the cross section would be violated. So the rise has to stop, and the proton is said to be saturated. The gluon distribution is the interesting part. It is not possible to investigate gluons from proton straight away because gluon have no charge, neither color.

One way to look at the gluon distribution is measuring the cross section of photonuclear reactions because the cross section is dependent on the square of the gluon distribution function; $\sigma \sim xG^2(x, Q^2)$ [17].

The photonuclear interactions can be studied in ultra-peripheral collisions (UPCs) of heavy ions (Pb–Pb) at the LHC. UPCs are characterized by an impact parameter larger than the sum of the radii of the two colliding nuclei. Because of the strong electromagnetic field, each nucleus is accompanied by a flux of virtual photons which is proportional to Z^2 where Z is the electric charge of the nucleus. The virtual photon can interact with either the whole nucleus (coherent interaction), thus the nucleus stays intact, or the photon interacts with a single nucleon (incoherent interaction) and the nucleus usually breaks up. The requirement for the coherent photoproduction constraints the mean transverse momentum of the vector mesons to be of the order of $p_T \approx 60 \text{ MeV}/c$. For the incoherent production the momentum transfer is higher because the nucleon radius is smaller than the radius of the nucleus, of the order of $p_T \approx 500 \text{ MeV}/c$.

An interesting photonuclear interaction is exclusive vector meson production. In exclusive production, only a vector meson is produced in the final state, and nothing else. In this thesis, the exclusive photoproduction of J/ψ with emission of forward neutrons is studied. The data were taken by ALICE in Pb–Pb ultra-peripheral collisions at $\sqrt{s_{NN}} = 5.02 \text{ TeV}$. Owing to the intense electromagnetic field, additional independent

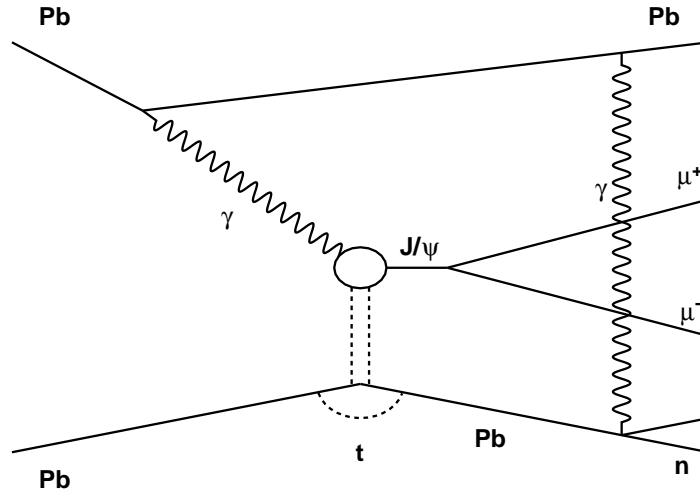


Figure 1.1: Feynman diagram for the photoproduction of a J/ψ vector meson with the emission of forward neutron.

electromagnetic interactions can occur between the nuclei and then one of the nucleus can emit forward neutrons, see Fig. 1.1. Different number of such neutrons can be emitted. Studying the differences according to the number of emitted forward neutrons is considered as a tool to decouple low- x and high- x contributions in vector meson photoproduction [18].

The J/ψ meson produced in Pb-Pb UPCs was studied at the LHC by the ALICE collaboration [1, 2]. Only the CMS collaboration measured the J/ψ production with neutron emission [3]. One chapter of this thesis is dedicated to the previous measurements of J/ψ production.

The specific objectives of this thesis are to:

- Produce the invariant mass distributions of dimuon pair in different rapidity bins and find J/ψ candidates.
- Study the energy distribution of the emitted forward neutrons Zero Degree Calorimeters (ZDC) for the selected events.
- Study the photoproduction of coherently produced J/ψ with different number of additionally emitted forward neutrons detected in the ZDCs.

Chapter 2 is dedicated to an introduction of nucleon structure, saturation and nuclear shadowing. Ultra-peripheral collisions, the cross section of the exclusively photoproduced J/ψ and a model describing the determination of the cross section are described in Chapter 3. The formulas for the inclusion of a different number of emitted neutrons is also covered, pursuant the article [9]. Chapter 4 is dedicated to the description of detectors that were used for this thesis. The previous measurements are summarized in Chapter 5. In Chapter 6 my own work is presented. In the very last Chapter 7 the conclusion and the outlook is summarized.

Chapter 2

Structure of nucleon

The observation of the fact that the proton is not a point-like object is attributed to a group lead by Robert Hofstadter from Stanford University. The group worked on the investigation of the structure of nuclei and also of nucleons. Hofstadter was awarded the Nobel prize for physics for his published results in 1961.

2.1 First experiments

In the experiments they used an electron beam accelerated up to 150 GeV with a linear accelerator (LINAC) hitting different kinds of nuclei and nucleons used as a target. Investigations of the structure of nuclei have showed that nuclei have a finite size but without a sharp boundary. Later on, the group started a series of experiments to investigate the structure of nucleons. The results from these experiments have shown that the proton does not behave as a pointlike object. Let's have a look on Fig. 2.1. The observed differential cross section of the measured elastic electron-proton scattering in dependence on the scattering angle (in degrees) is shown and it is compared with theoretical calculations. Dirac curve corresponds to the idea of a pointlike proton, the anomalous curve takes account of the magnetic moment of the proton and the last curve is the Mott cross section. Experimental data was fitted by the Mott cross section multiplied by the form factor and it lead to the determination of the root-mean-square radius of the proton $r = 0.7 \pm 0.24$ fm. So the conclusion was that the proton is a particle with a finite radius of the order of 1 fm.

Thanks to the results from electron-proton scattering experiments it was decided to build a new electron accelerator, the Stanford Linear Accelerator Center (SLAC). The electron beam energy could reach up to 20 GeV. In the late sixties, a group of physicists from SLAC and the Massachusetts Institute of Technology (MIT) started a series of experiments studying not only elastic electron-proton scattering, but also the first serious study of deep inelastic electron-proton scattering (DIS).

In DIS experiments a lepton probes a target nucleon or nucleus via the exchange of an electroweak boson. In deep inelastic scattering an elementary particle (lepton) transfers large energy-momentum to a nucleon, which then breaks up. Essentially a quark is knocked out of the nucleon and the quark hadronizes then, the scheme of the process is shown in Fig. 2.2. The interacting electron emits a virtual photon $\gamma^*(q)$, which is then absorbed by one of the quarks, which is in the proton. During the short time of the interaction, quarks behave as free particles. The participating quark carries

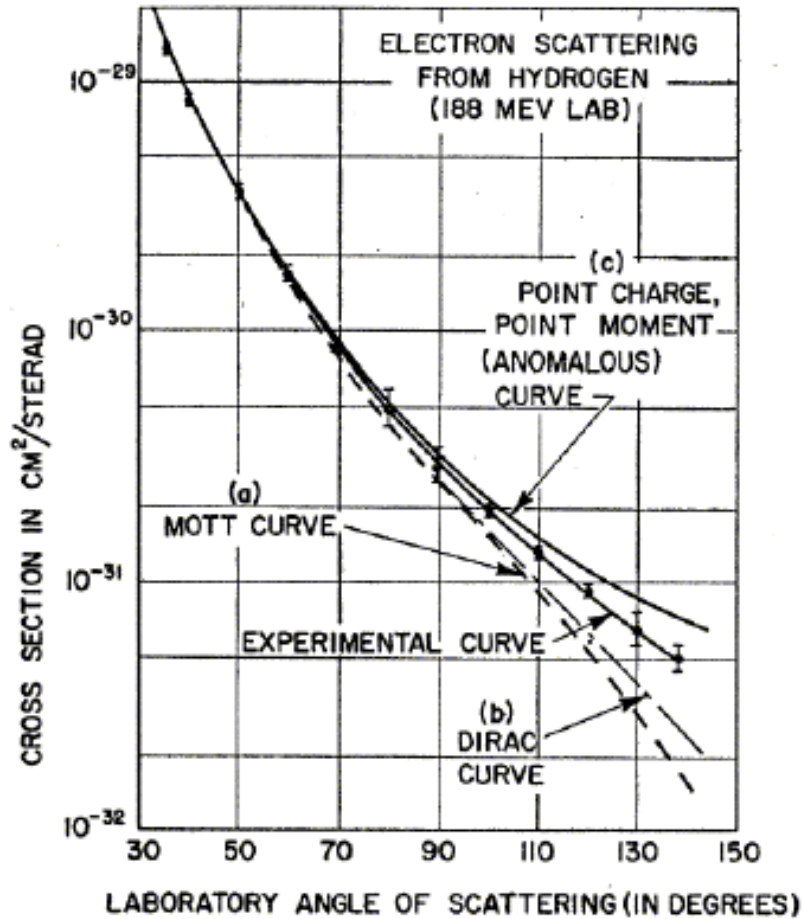


Figure 2.1: The measured differential cross section in comparison with theoretical calculations [4].

a fraction of longitudinal momentum of the whole proton x and can be considered as a real massless particle.

Bjorken proposed that the structure functions that describe the cross sections for the inelastic electron scatterings satisfy a scaling property known as Bjorken scaling. There are two Lorentz invariant kinematic variables for DIS. The structure functions depend on these two variables. Bjorken scaling means that in a large momentum transfer Q^2 , these structure functions become a function of the ratio of the two variables. Experiments made at SLAC confirmed the Bjorken scaling and Feynman formulated the parton model based on this idea [19]. The kinematics of the DIS process is recalled next.

The variables are referred to P - proton momentum, k - momentum of real massless interacting quark, q - momentum of the virtual photon γ^* and s is the photon-proton invariant mass.

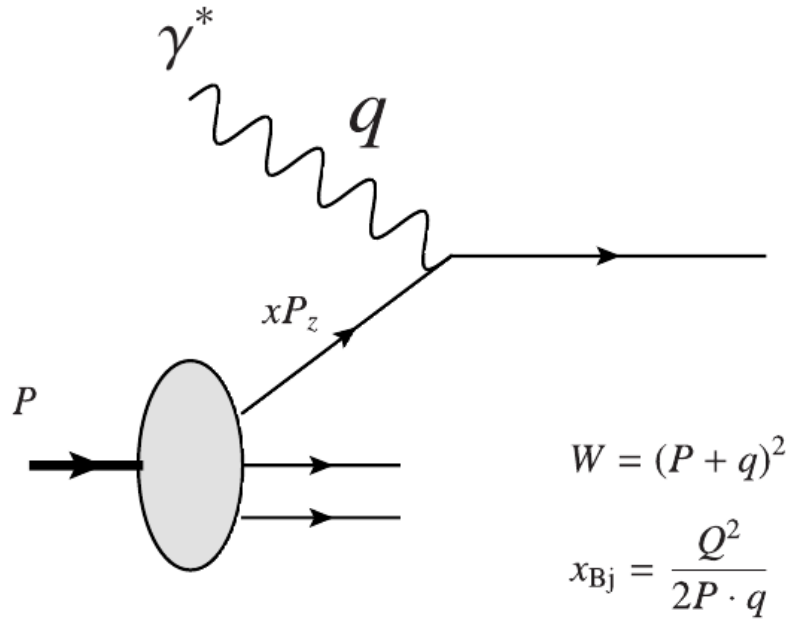


Figure 2.2: Deep inelastic scattering of an electron on a proton, in the Bjorken frame where the proton has very large energy while the virtual photon γ^* has small longitudinal momentum. In the Bjorken frame, also called the infinite momentum frame, the mass of the proton can be ignored as well as the mass of its constituents, the valence quarks.

$$k^2 = 0 = (k + q)^2 \text{ or } q^2 + 2k \cdot q = 0 \quad (2.1)$$

then setting:

$$k = xP, Q^2 = -q^2 > 0 \quad (2.2)$$

one gets:

$$x = x_{Bj} = \frac{Q^2}{(2P \cdot q)} \approx \frac{Q^2}{(s + Q^2)} \quad (2.3)$$

the approximation is valid because of the proton mass is neglected.

The DIS experiments extract information from the lepton scattering cross section to measure Structure Functions of the target, which are directly related to the PDFs [16]. The question was, how the structure functions $F_i(x, Q^2)$ behave with increasing Q^2 . It was expected that they would be a constant function of x , unlike the elastic scattering, which goes rapidly to zero with increasing Q^2 .

The first MIT-SLAC results on the elastic and inelastic electron-proton scattering were reported in 1968. The results brought up a question: 'What are nucleons made of?' and it had attracted the attention of Feynman, Bjorken and other theorists. Feynman based his parton model on these results.

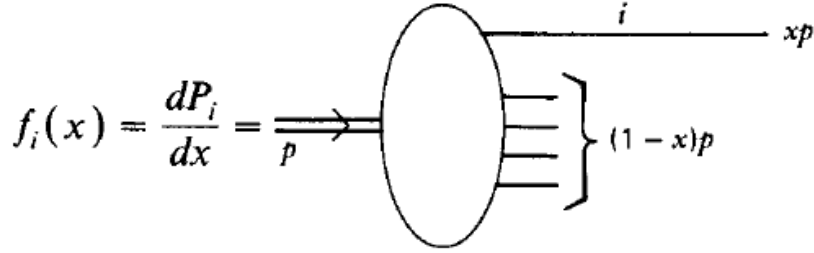


Figure 2.3: The parton momentum distributions f_i describe the probability that the struck parton i carries a fraction x of proton's momentum P [5].

2.2 Feynman's parton model

Deep Inelastic Scattering played a decisive role in formulating the parton model [6]. The model is valid in the infinite momentum frame, or Bjorken frame, in which the longitudinal momentum of the moving proton is much larger than the mass of proton, therefore the mass can be neglected. Feynman suggested that nucleons consisted of point-like constituents, called partons. For the formulation of the parton model, parton distribution function were used. The partons inside a proton can each carry a different fraction x of the proton's momentum and energy. The probability that the interacting parton i carries a fraction x is describe by the parton momentum distribution f_i , as shown in Fig. 2.3. Partons i refer to the charged partons, which interact with the photon, but it has to be taken into consideration that the proton might contain non-charged partons, which do not interact with the photon. Then all fractions x of all partons i' , both charged and non-charged, sum up to 1; therefore,

$$\sum_{i'} \int dx x f_{i'}(x) = 1. \quad (2.4)$$

The dimensionless structure function at large Q^2 , with

$$x = \frac{1}{\omega} = \frac{Q^2}{2M\nu}$$

become

$$F_2(x) = \sum_i e_i^2 x f_i(x), \quad (2.5)$$

and

$$F_1(x) = \frac{1}{2x} F_2(x). \quad (2.6)$$

After some calculations the master formula of the parton model can be obtained:

$$2xF_1(x) = F_2(x) = \sum_i e_i^2 x f_i(x). \quad (2.7)$$

The parton model result $2xF_1 = F_2$ is called the Callan-Gross relation and it is a consequence of the quarks having spin $1/2$. The relation is well satisfied by data.

A series of experiments on DIS were made measuring the structure function $F_2(x)$ and the results brought the following. Studying the momentum distribution of the

quarks inside the proton brought the information that quarks carry less than half of the momentum of the proton:

$$\varepsilon_u = 0.36,$$

$$\varepsilon_d = 0.18.$$

The remaining almost 50% of the momentum of the proton is carried by the electrically neutral gluons:

$$\varepsilon_g = 0.46.$$

2.3 Saturation

DIS of electrons on protons have provided information about the distributions of low- x partons [6]. The PDFs were measured by the ZEUS and H1 collaborations at DESY and the results are shown in Fig. 2.4 where one can read that at large values of x the valence quarks dominate. Their densities are denoted $xu(x)$ for u quark and $xd(x)$ for d quark. However, at small x , gluons and sea quarks, described as $xg(x)$ and $xS(x)$ dominate. Gluons represent the largest parton density. Note that the gluon and sea quark distributions are scaled down by a factor of 20. The information at very low- x provides strong evidence, that the gluon density increases rapidly with lower x . However this growth cannot go on forever because it would, at some point, violate the unitarity of the scattering matrix. At the moment when the gluon density is large enough, a recombination processes enter the foreground and the radiation of softer and softer gluons is balanced. This leads eventually to saturation. Saturation is characterized by a transverse momentum scale Q_s ; the saturation momentum. Small x partons with large transverse momenta fill a small transverse size, on the contrary partons with small transverse momenta occupy a large transverse size and will eventually overlap as their number increases. When the entire transverse plane is densely packed with partons, which have transverse momenta smaller than Q_s , the system is saturated. The value of Q_s grows with the energy of the collision and the size of the participants in a collision. Typical values for large nuclei are $Q_s^2 \approx 5 \text{ GeV}^2$ at the LHC. At high energy, the saturation momentum is the only relevant scale so it controls the magnitude of the QCD coupling constant.

2.4 Nuclear shadowing

Nuclear shadowing [20] in the nuclear structure functions has been predicted on the basis of the parton model. The shadowing is a result of parton recombination, therefore we can talk about it as about unitarity corrections. Shadowing effects exist in the proton structure function as well, however there is no direct way to experimentally observe shadowing in the proton because there is nothing to compare to. The shadowing effects are expected to be significant at small- x values.

For structure function F_2 , the nuclear ratio is defined as the nuclear structure function per nucleon divided by the nucleon structure function [7]:

$$R_{F_2}^A(x, Q^2) = \frac{F_2^A(x, Q^2)}{AF_2^{\text{nucleon}}(x, Q^2)}. \quad (2.8)$$

In the equation A refers to the nuclear mass number. The nucleon structure function F_2^{nucleon} is measured by scattering on deuterium, where the nuclear effects are assumed

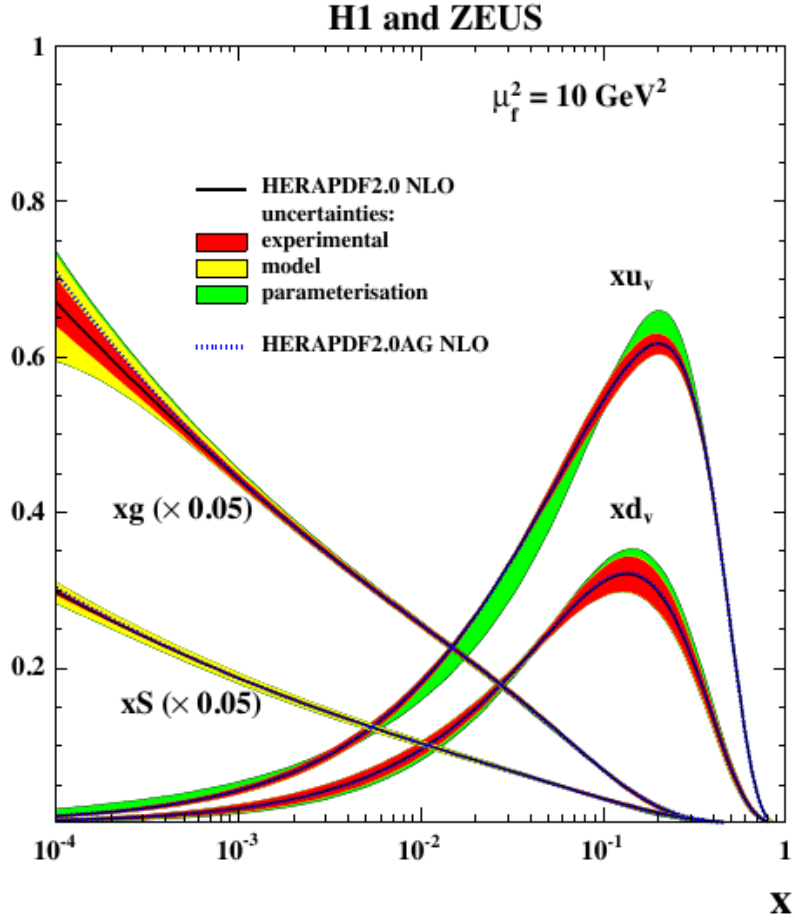


Figure 2.4: The parton distribution functions of a proton in dependence on x , measured at HERA [6].

to be negligible

$$F_2^{\text{nucleon}} = F_2^{\text{deuterium}}/2.$$

The ratio $R_{F_2}^A(x, Q^2)$ is measured as a function of x for a fixed Q^2 and the behavior is illustrated in Fig. 2.5. The region of nuclear shadowing is $R_{F_2}^A(x, Q^2) < 1$ for $x \lesssim 0.1$. Data shows that the shadowing increases with decreasing x . However, when the value of x is the lowest available, the behavior is consistent with saturation. Experiments also showed that the shadowing increases as the mass number A of the interacting nucleus grows. However, with increasing Q^2 the shadowing decreases. Since at small- x the partons of different nucleons overlap in nuclei, larger partons densities are expected, and consequently stronger shadowing than in protons.

A way to study the nuclear gluon shadowing is measuring vector meson production in Ultra-Peripheral Collisions (UPCs), which are discussed in the next chapter.

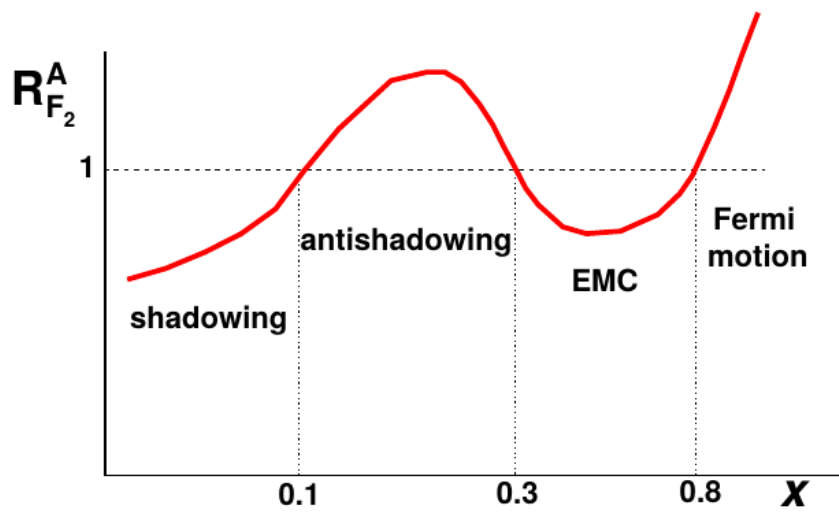


Figure 2.5: Schematic behavior of the ratio $R_{F_2}^A(x, Q^2)$ in dependence on x for a fixed Q^2 [7].

Chapter 3

Exclusive coherent photoproduction of a J/ψ in ultra-peripheral collisions

3.1 Ultra-peripheral collisions

Because of Lorentz contraction, the two colliding nuclei appear, in the center-of-mass frame of the collision, as two contracted pancakes, with a thickness of a small fraction of a femtometer ($\approx 10^{-3}$ fm at the LHC), while the diameter of a Pb nucleus is about 12 fm [21]. The electromagnetic field of the charged Pb nuclei can be treated as a flux of virtual photons. The intensity of the photon flux is proportional to Z^2 . In ultra-peripheral collision (UPC) nuclei interact via these photons. The impact parameter b is larger than the sum of radii of the nuclei. A purely hadronic interaction is excluded by the distance in impact parameter because of the short range of the strong force, therefore only electromagnetic induced interaction can occur. A schematic view of such collision is shown in Fig. 3.1. The whole nucleus coherently emits photons, therefore setting a limit on the minimum photon wavelength being larger than the nuclear radius. The uncertainty principle imposes an upper limit on the transverse momentum of the radiated photon in the transverse plane, such as $p_T \lesssim \hbar c/R_A \approx 28$ MeV/ c for Pb beam. In the longitudinal direction, where there is Lorentz contraction, the maximum possible momentum is multiplied by a Lorentz factor γ_L , then $k \lesssim \hbar c \gamma_L/R_A$.

Different types of reactions can occur in UPCs and they are illustrated in Fig. 3.2. When one radiated photon interacts with another one it is called photon-photon collision, Fig. 3.2(a). In photon-nuclear collisions, the radiated photon interacts with a whole nucleus or with a constituent of the other nucleus, Fig. 3.2(b). In these two types of collisions the nucleus emitting the photon remains usually intact after the collision. When an additional photon is emitted and it interacts, a breakup of one or both nuclei can occur, as shown in Fig. 3.2(c).

3.2 Exclusive photonuclear process

One possible type of photonuclear interaction is exclusive vector meson production [22]. That is a reaction where only a vector meson is produced, and nothing else. This pro-

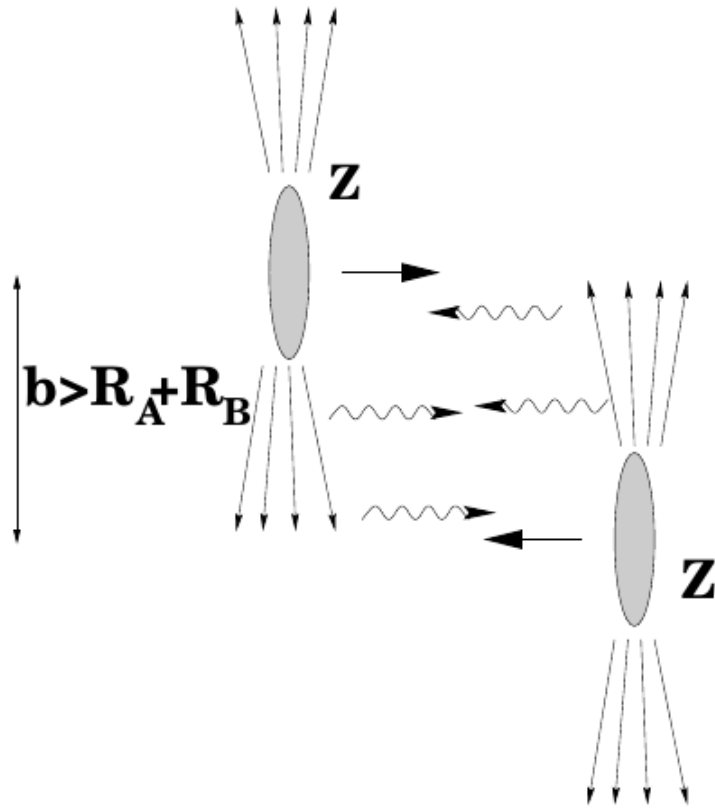


Figure 3.1: Schematic illustration of an ultra-peripheral collision of two nuclei, two contracted pancakes. The impact parameter of the collision b is larger than the sum of the two radii, R_A and R_B [8].

cess has a large cross section. This type of photonuclear reaction, called photoproduction, can occur in different forms. We talk about coherent production, when the photon interacts coherently with the whole nucleus. The coherence condition sets the limit of the transverse momentum of the produced vector meson - $p_T \sim 1/2R_{pb} \sim 60 \text{ MeV}/c$. When another photon from the cloud of photons of nucleus interacts additionally with the other nucleus, one of the nucleus might breakup. In incoherent production the photon interacts with a single nucleon inside the nucleus and the target nucleus breaks up in almost all cases. The transverse momentum of the produced particle is larger, $p_T \sim 300 \text{ MeV}/c$.

Exclusive coherent photoproduction of J/ψ can be used as a probe of the gluon distribution of the target nuclei $g(x, \mu^2)$ at a small momentum fraction x and the resolution scale of few GeV^2 for J/ψ . In this section the cross section of the exclusive photoproduction with emission of forward neutrons is described.

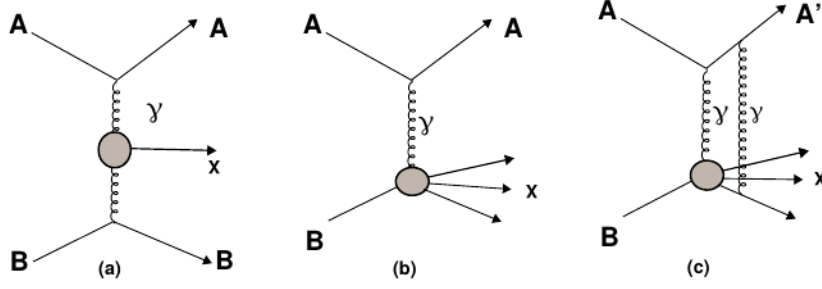


Figure 3.2: Different types of reactions possible in UPCs, (a)-photon–photon collision, (b)-photonuclear collision and (c)-photonuclear reaction with nuclear breakup due to additional photon exchange [8].

3.3 Cross section

The cross section for exclusive photoproduction of J/ψ in Pb–Pb UPCs is the sum of two contributions [9]:

$$\frac{d\sigma_{PbPb \rightarrow J/\psi PbPb}(y)}{dy} = N_{\gamma/Pb}(y)\sigma_{\gamma Pb \rightarrow J/\psi Pb}(y) + N_{\gamma/Pb}(-y)\sigma_{\gamma Pb \rightarrow J/\psi Pb}(-y), \quad (3.1)$$

where y is the rapidity of the vector meson J/ψ ,

$$N_{\gamma/Pb}(y) = \omega dN_{\gamma/Pb}(\omega)/d\omega$$

is the photon flux of the Pb ion; $\sigma_{\gamma Pb \rightarrow J/\psi Pb}(y)$ is the cross section of exclusive photoproduction of J/ψ on the hadronic target Pb . The rapidity y is related to the photon energy in the laboratory reference frame ω as:

$$\omega = \frac{M_{J/\psi}}{2} e^{\pm y} \quad (3.2)$$

where $M_{J/\psi}$ is the mass of J/ψ .

The two terms occurring in Eq. 3.1 reflect a specific feature of UPCs: each colliding nucleus can behave as a target of the collision or it can be the one, that radiates the interacting photon. From Eq. 3.2 we can see that for each value of rapidity, there are two possible contributions to J/ψ production. Contribution of photon interacting with low energy: $\omega_L = \frac{M_{J/\psi}}{2} e^{-y}$ and the other possibility, that photon interacts with high energy $\omega_H = \frac{M_{J/\psi}}{2} e^y$.

For the case when $y = 0$, one obtains:

$$\sigma_{\gamma Pb \rightarrow J/\psi Pb}(y = 0) = \frac{d\sigma_{PbPb \rightarrow J/\psi PbPb}(y = 0)}{dy} / (2N_{\gamma/Pb}(y = 0))$$

A J/ψ produced in a certain rapidity y is sensitive to the gluon distribution at

$$x = \frac{M_{J/\psi}}{\sqrt{s_{NN}}} \exp(\pm y)$$

at hard scale; $Q^2 \approx \frac{M_{J/\psi}^2}{4}$.

The photon flux of the Pb ion $N_{\gamma Pb}(\omega)$ in dependence on the energy of the photon can be obtained using the Weizsäcker–Williams approximation of quantum electrodynamics and it can be calculated with the uncertainty of the order of 5%. The expression for the $N_{\gamma Pb}(\omega)$ is:

$$N_{\gamma/Pb}(\omega) = \int d^2\vec{b} \Gamma_{PbPb}(b) N_{\gamma/Pb}(\omega, b), \quad (3.3)$$

where b is the impact parameter. In the Pb–Pb UPCs we need to take into account the required suppression of the strong interaction between nuclei then $\Gamma_{PbPb}(b)$ is the probability that there is no strong interaction between interacting ions at the impact parameter b . And the last term, $N_{\gamma/Pb}(\omega, b)$, is the photon flux of Pb ion depending on the impact parameter b .

The Glauber model describes the high-energy nucleus–nucleus scattering and the probability $\Gamma_{PbPb}(b)$ is given by the expression

$$\Gamma_{PbPb}(b) = \exp\left(-\sigma_{NN}^{\text{tot}} \int d^2\vec{b}_1 T_{Pb}(\vec{b}_1) T_{Pb}(\vec{b} - \vec{b}_1)\right), \quad (3.4)$$

where σ_{NN}^{tot} is the total nucleon–nucleon cross section, $T_{Pb}(b) = \int dz \rho_{Pb}(b, z)$ is the nuclear optical density, where ρ_{Pb} is the density of nucleons.

The photon flux $N_{\gamma/Pb}(\omega, b)$ is given by the expression:

$$N_{\gamma/Pb}(\omega, b) = \frac{\alpha_{\text{e.m.}} Z^2}{\pi^2} \left| \int_0^\infty \frac{dk_\perp k_\perp^2}{k_\perp^2 + \omega^2/\gamma_L^2} F_{\text{ch}}(k_\perp^2 + \omega^2/\gamma_L^2) J_1(bk_\perp) \right|^2, \quad (3.5)$$

where $\alpha_{\text{e.m.}}$ is the fine-structure constant, Z is the charge of the ion emitting the photon and $F_{\text{ch}}(k_\perp^2)$ is the charge form factor of the ion emitting the photon, k_\perp is the photon transverse momentum and J_1 is the Bessel function of the first kind.

The coherent photoproduction of J/ψ in Pb–Pb UPCs can be accompanied by an additional electromagnetic interaction of the interacting ions. Multiple photon exchanges between the colliding ions lead to excitation of one or both nuclei and then forward neutron emission follows. Such neutrons can be detected by zero degree calorimeters (ZDCs) which are placed on both sides of the detector at long distance, see section 4.3. Assuming that all photon emissions are independent, these additional electromagnetic interactions affect the photon flux $N_{\gamma Pb}(\omega)$ as [25].

$$N_{\gamma/Pb}^i(\omega) = \int d^2\vec{b} P_i(b) \Gamma_{PbPb}(b) N_{\gamma/Pb}(\omega, b), \quad (3.6)$$

where $P_i(b)$ is the probability of Coulomb excitation at the impact parameter b in channel i ;

$$i = (0n0n, 0nXn, XnXn)$$

label various channels corresponding to a different number of neutrons detected in both ZDCs. For example, the channel 0n0n corresponds to the case when ZDCs on both sides are empty, the 0nXn-channel corresponds to detection of no neutron in one ZDC and at least one neutron detected in the other ZDC. The last XnXn-channel corresponds to detection of at least one neutron in each ZDC detector.

3.4 Exclusive photoproduction of charmonia on nuclei in LO perturbative QCD

In this section a prediction for vector meson photoproduction cross section in UPC based on the Leading Order perturbative QCD (LO pQCD) is presented. It was presented in the paper [9].

The cross section of the exclusive photoproduction of vector meson in the lowest Fock state on the the proton is

$$\frac{d\sigma_{\gamma p \rightarrow V p}(W_{\gamma p}, t=0)}{dt} = C_p(\mu^2) [\alpha_s(\mu^2) x g_p(x, \mu^2)]^2, \quad (3.7)$$

where V stands for a vector meson, $\alpha_s(\mu^2)$ is the strong coupling constant; $x g_p(x, \mu^2)$ is the gluon density of the proton evaluated at the light-cone momentum fraction $x = M_V^2/W_{\gamma p}^2$ and the resolution scale μ ; $C_p(\mu^2)$ is the normalization factor depending on approximations used in the evaluation of the $\gamma p \rightarrow P b p$ amplitude. In the case of J/ψ production on a proton, it was found that $\mu^2 = M_{J/\psi}^2/4 = 2.4 \text{ GeV}^2$ and

$$C_p(\mu^2) = \pi^3 \Gamma_{ee} M_{J/\psi}^3 / (48 \alpha_{\text{e.m.}} \mu^8),$$

where Γ_{ee} is the decay width of the J/ψ decay to an electron-positron pair, $\alpha_{\text{e.m.}}$ is the fine-structure constant. To get more accurate results, one gets beyond this approximation and do some corrections:

$$C_p(\mu^2) = F^2(\mu^2) \bar{R}_g^2 (1 + \eta^2) \pi^3 \Gamma_{ee} M_{J/\psi}^3 / (48 \alpha_{\text{e.m.}} \mu^8),$$

where η is the ratio of the real to the imaginary parts of the $\gamma p \rightarrow J/\psi p$ scattering amplitude and $\bar{R}_g \approx 1.2$ is the skewedness factor. The skewedness factor describes the increase of the $\gamma p \rightarrow J/\psi p$ amplitude due to its off-forward kinematics, and $F^2(\mu^2) \approx 0.5$ is the factor taking into account the effects of the charm quark transverse momentum in the J/ψ wave function. Because the charm quark has nonzero transverse momentum, the resolution scale μ^2 of the probe increases. Therefore, the resolution scale for J/ψ and $\Psi(2S)$ is obtained to be $\mu^2 \approx 3 \text{ GeV}^2$ and $\mu^2 \approx 4 \text{ GeV}^2$, respectively. The approach based on Eq. 3.7 provides a good agreement of high-energy HERA and LHC measurements of charmonium photoproduction off a proton.

The Eq. 3.7 can be applied to a nuclear target and the corresponding cross section follows:

$$\begin{aligned} \sigma_{\gamma A \rightarrow J/\psi A}(W_{\gamma p}) &= C_A(\mu^2) [\alpha_s(\mu^2) x g_A(x, \mu^2)]^2 \Phi_A(t_{\min}) \\ &= \frac{C_A(\mu^2)}{C_p(\mu^2)} \frac{d\sigma_{\gamma p \rightarrow J/\psi p}(W_{\gamma p}, t=0)}{dt} \\ &\quad \left[\frac{x g_A(x, \mu^2)}{A x g_p(x, \mu^2)} \right]^2 \Phi_A(t_{\min}), \end{aligned} \quad (3.8)$$

where $x g_A(x, \mu^2)$ is the nuclear gluon distribution; $\Phi_A(t_{\min}) = \int_{-\infty}^{t_{\min}} dt |F_A(t)|^2$, where $F_A(t)$ is the nuclear form factor; $t_{\min} = -x^2 m_N^2$ is the minimal momentum transfer squared, where m_N is the nucleon mass; $C_A(\mu^2)/C_p(\mu^2) = (1 + \eta_A^2) \bar{R}_{g,A}^2 / [(1 + \eta^2) \bar{R}_g^2] \approx 0.9$, where $\bar{R}_{g,A}$ and η_A are the skewedness and the ratio of the real to the imaginary parts of the $\gamma A \rightarrow VA$ scattering amplitude, respectively.

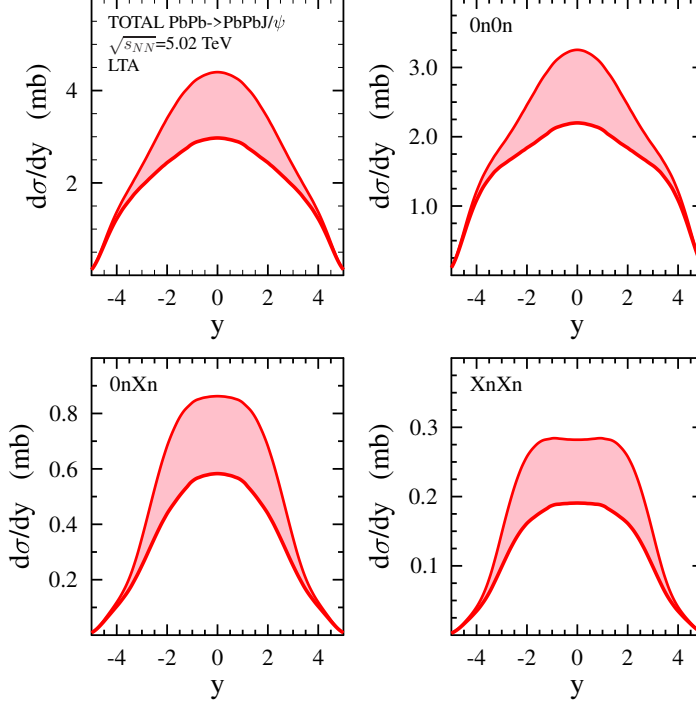


Figure 3.3: The $d\sigma_{PbPb \rightarrow J/\psi PbPb}(y)/dy$ cross section as a function of the J/ψ rapidity y at $\sqrt{s_{NN}} = 5.02$ TeV predicted by LO pQCD in Eq. 3.7 and Eq. 3.8 with the gluon shadowing ratio $R_g(x, \mu^2)$ of the leading twist nuclear shadowing model. The shaded areas span the range of predictions corresponding to the upper and lower limits on $R_g(x, \mu^2)$. The left upper plot shows the total cross section, the other plots show different neutron emission channels. Figure taken from [9].

Reading the Eq. 3.8, one can obtain the nuclear gluon shadowing, given by the ratio $R_g(x, \mu^2) = xg_A(x, \mu^2)/[Axg_p(x, \mu^2)]$, as it was described earlier. A nuclear suppression factor extracted from the ALICE measurements of exclusive J/ψ photoproduction, which will be discussed later on, was compared to the theoretical prediction based on Eq. 3.8. It provides a first model independent evidence of large nuclear shadowing at $x = 0.001$:

$$R_g(x = 0.001, \mu^2 = 3\text{GeV}^2) \approx 0.6.$$

In Fig. 3.3 and Fig. 3.4 $d\sigma_{PbPb \rightarrow J/\psi PbPb}(y)/dy$ as a function of the J/ψ rapidity y is presented. It represents the calculations of Eq. 3.7 and Eq. 3.8. Fig. 3.3 shows the results of the leading twist nuclear shadowing model for the ratio of the gluon shadowing $R_g(x, \mu^2)$ at a resolution scale of $\mu^2 = 3\text{GeV}^2$. The shaded areas demonstrate the reach within the limits of $R_g(x, \mu^2)$. Different channels of additional neutron emission are illustrated.

Similarly, the cross section prediction is demonstrated in Fig. 3.4 but the EPS09 model of nuclear parton distribution functions (PDFs) is presented. The shaded areas

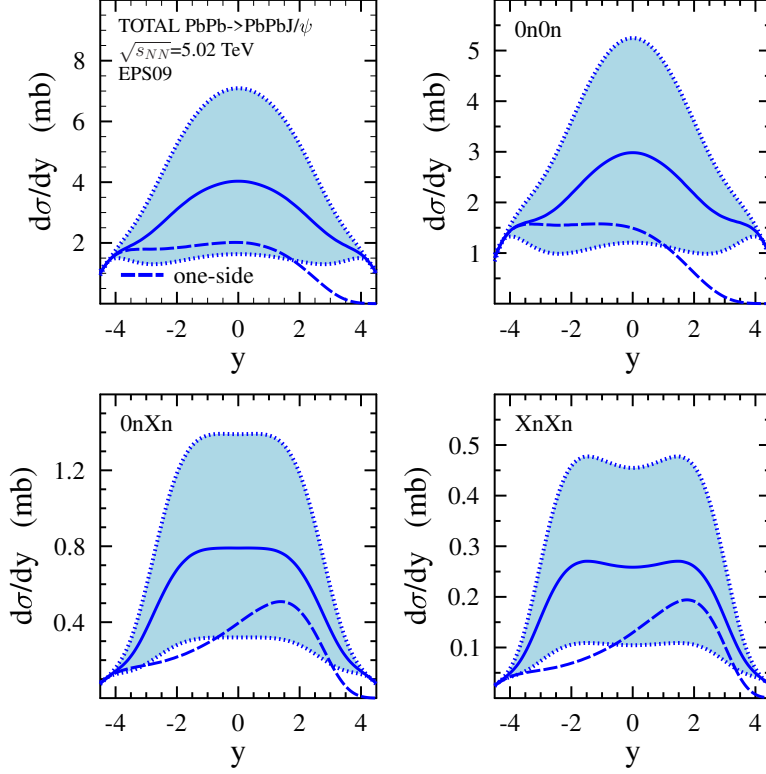


Figure 3.4: The prediction of $d\sigma_{PbPb \rightarrow J/\psi PbPb}(y)/dy$ cross section as a function of the J/ψ rapidity y at $\sqrt{s_{NN}} = 5.02$ TeV of LO pQCD with the EPS09 gluon shadowing ratio $R_g(x, \mu^2)$. The shaded areas show the uncertainties of $R_g(x, \mu^2)$. The dashed curves labeled "one-side" show the contribution of the first term in Eq. 3.1. Figure taken from [9]

represent the theoretical uncertainties of $R_g(x, \mu^2)$ in the EPS09 fit of the nuclear PDFs. The dashed lines illustrate the one-side contribution, reading the first term of Eq. 3.1. One can notice that one-side rapidity distributions are strongly different in variations of neutron channels. It is explained by the decrease of median impact parameter b contributing in equation for photon flux, Eq. 3.3, in 0nXn and XnXn - channels, it is due to electromagnetic excitation of the nuclei. This phenomenon leads to an increase of ω_H contribution to the photon flux $N_{\gamma/A}^i(\omega)$. And hence, the gluon distribution in nuclei $g_A(x, \mu^2)$ in the 0nXn and XnXn - channels can be probed in lower values of x than in "full" and 0n0n-channels.

Chapter 4

ALICE detector

The ALICE detector [26] is one of four main experiments at the Large Hadron Collider (LHC) located close to Geneva in Switzerland. The LHC is a 27 kilometers long synchrotron collider designed to collide proton or lead beams at very high energies. At such collisions many interesting particles are produced that allow us to study different states of matter. The ALICE experiment is designed to look on the state of matter that is called the Quark Gluon Plasma (QGP) and to measure its properties.

The ALICE detector has overall dimensions of $16 \times 16 \times 26\text{m}^3$. It consists of a central barrel part which covers polar angles from 45° to 135° and it is embedded in a large solenoid magnet and it is shown in Fig. 4.1. The central barrel contains the Inner Tracking System (ITS), Time-Projection Chamber (TPC), Time-of-Flight (TOF), Ring Imaging Cherenkov (HMPID) and Transition Radiation (TRD) detectors, and two electromagnetic calorimeters (PHOS, EMCal). Several smaller detectors are located at small angles, such as ZDC, AD, and V0.

In the next sections, important detectors for this analysis are described in more detail. Another subdetectors of ALICE were described in my bachelor thesis [27].

4.1 Inner Tracking System (ITS)

The ITS [11] surrounds the beam pipe. It is the main contributor for measuring the primary vertex of the collision. It is located at radius between 4 and 43 cm around the beam pipe. The detector layout has been designed taking into account the high multiplicity environment foreseen for central Pb–Pb collisions, so that occupancy is kept on the order of a few percent.

The ITS consists of six layers of position sensitive semiconductor detectors; Silicon Pixel Detectors (SPD), Silicon Drift Detectors (SDD) and Silicon Strip Detectors (SSD). Each type of detector consists of two layers and its scheme is shown in Fig. 4.2.

The SPD, the two innermost layers of the ITS, is aimed to determine the position of the primary vertex of the collision with a resolution better than $100\mu\text{m}$. It has $9.8 \cdot 10^6$ readout channels. The SPD consists of 240 modules with 1200 readout chips. The SPD is very highly segmented so it has also been used for the triggering of the UPC processes at mid-rapidity.

The Silicon Drift Detector (SDD) is based on modules with a sensitive area of $70.17(r\phi) \cdot 75.26(z)\text{mm}^2$, divided into two drift regions where electrons move in opposite directions under a drift field of approximately 500 V/cm. The modules are mounted

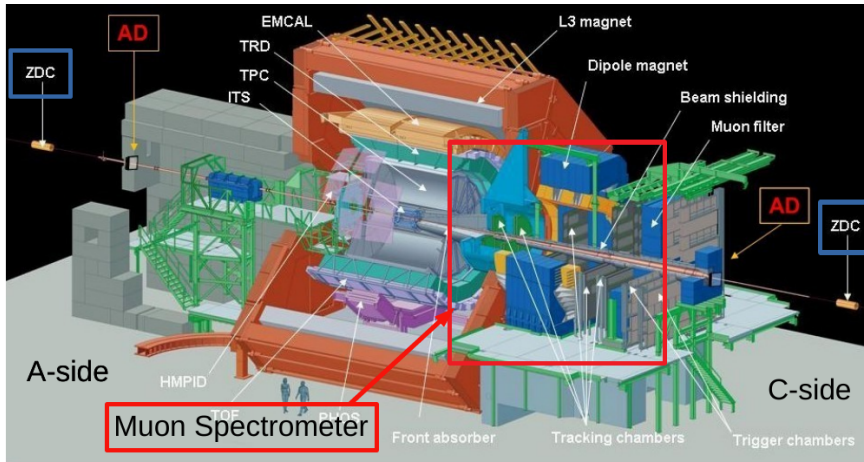


Figure 4.1: Schema of the ALICE detector with important subdetectors for this work highlighted [10].

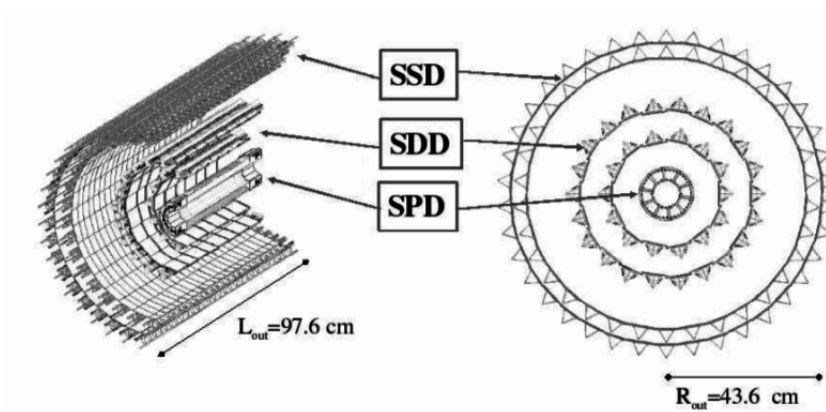


Figure 4.2: The layout of the Inner Tracking System [11].

into ladders, the inner layer is structured in 14 ladders with 6 modules each and the outer layer of SDD is composed of 22 ladders with 8 modules each of them. The position of the particles along the z axis is reconstructed from the centrist of the collected charge along the anodes and the position along the drift r coordinate is determined from the measured drift time with respect to the trigger time. A precise knowledge of the drift speed is needed for this reconstruction. The drift speed is measured during calibration runs.

The two outermost ITS layers form the Silicon Strip Detector (SSD) which is a module consisting of one double-sided strip detector connected to two hybrids hosting the front-end electronics. The sensors have an active area of $73(r) \cdot 40(z) \text{ mm}^2$ and they are $300 \mu\text{m}$ thick. Each sensor has 768 strips on each side which are almost parallel to the z axis direction. The innermost layer of the SSD is composed of 34 ladders with 22 modules each. The outer layer is made of 38 ladders, each of them is composed of 25 modules.

A high resolution on the impact parameter is important to reconstruct secondary

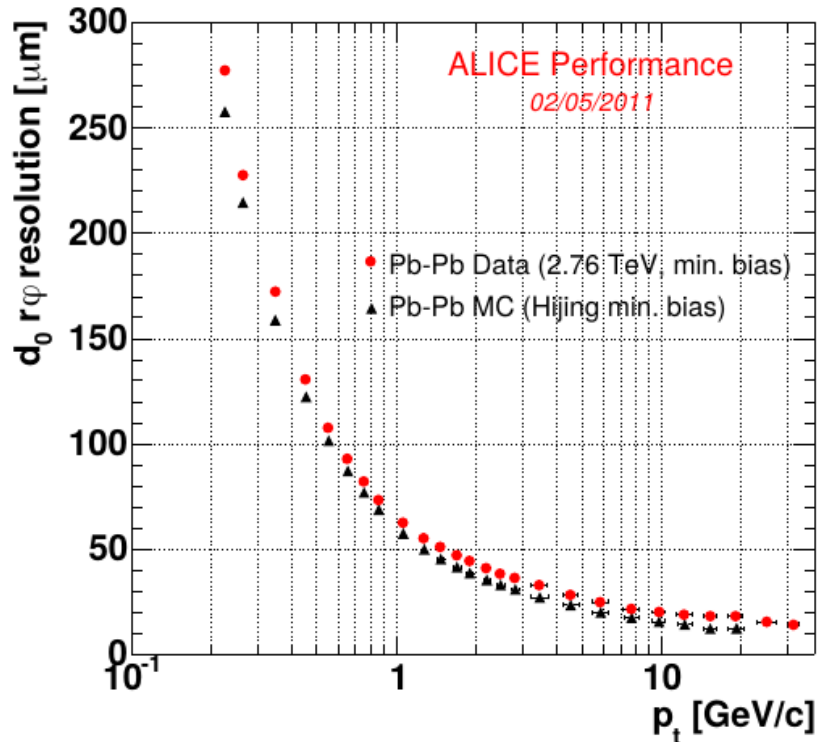


Figure 4.3: Transverse impact parameter resolution in dependence on p_T [11].

vertices from hyperons and heavy flavour meson decays. In Fig. 4.3, the transverse impact parameter resolution is shown as a function of p_T , measured in 2010 Pb-Pb collisions. The resolution is obtained for tracks with two signals in the SPD. The resolution in the $r\phi$ plane is nearly $50\mu\text{m}$ for particles with momentum 1 GeV. With higher momentum the resolution decreases.

The four outer layers have analogue readout, therefore they can be used for particle identification via dE/dx measured in the non-relativistic region for low momentum particles ($p_T > 100$ MeV). Electrons can be identified from 80 MeV/c up to 160 MeV with 2σ separation from π . Pions are separated from kaons up to 0.6 GeV and kaons from protons up to 0.8 GeV.

4.2 Muon Spectrometer

The main function of the Muon Spectrometer is to measure open flavor production and quarkonia production, such as J/ψ , via their decay into muons. For nucleus-nucleus collisions the centrality dependence with the reaction plane can be studied. The Muon Spectrometer covers the rapidity range of $-4.0 < y < -2.5$ and the acceptance for J/ψ meson is presented in Fig. 4.4. Two experimental requirements for the muon detector are to measure quarkonia production at very low p_T and to have an invariant mass resolution of the muon spectrometer about 100 MeV to distinguish different resonances of the Υ family. The muon spectrometer is located on the C-side of the ALICE experiment

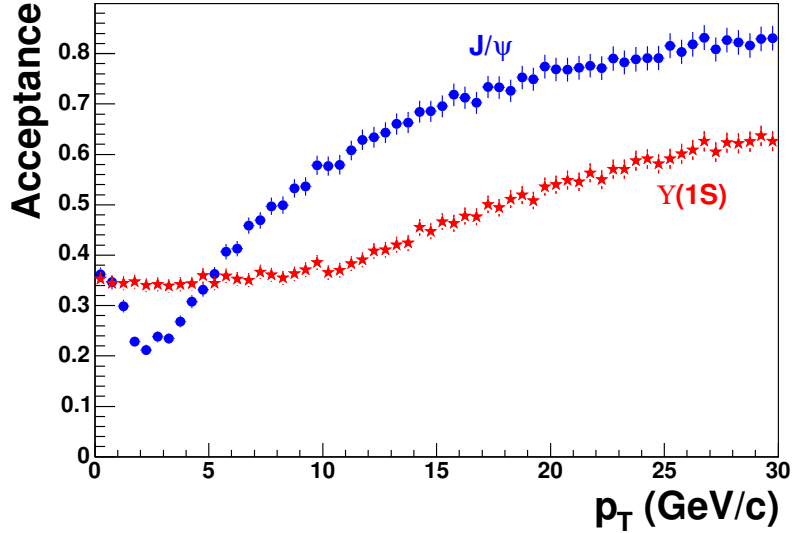


Figure 4.4: Acceptance of the Muon Spectrometer as a function of p_T of J/ψ and $Y(1S)$ in the muon spectrometer rapidity range in their dimuon decay channel with a muon low p_T cut equal to 1 GeV [12].

and it covers the angular range $171^\circ < \theta < 178^\circ$. It consists of three absorbers, a muon magnet, a trigger system and a tracking system. The layout of the detector is presented in Fig. 4.5 [12]. In the following text, the individual parts of the muon spectrometer are described [13].

4.2.1 Absorbers

The front absorber decreases the forward flux of charged particles by at least two orders of magnitude and also decreases the muon background from the decay of pions and kaons. It is achieved by minimizing the distance between the interaction point to the absorber to 90cm. To provide a good shielding and limited multiple scattering low- Z material is used in the layers closer to the interaction point and materials with higher Z are used to shield further in the movement direction. In Fig. 4.6 the layout of the muon spectrometer with different materials used is shown.

4.2.2 Dipole magnet

The muon spectrometer dipole magnet provides a maximum central field of 0.7T and an integral field of 3Tm. The coils are cooled with water to a temperature about 15 – 25°C and its overall dimensions are 5 meters in length, 7.1 m width and 9 m height. The dipole has the same angular acceptance of the detector and provides a horizontal magnetic field perpendicular to the beam axis. The polarity of the field can be reverted in a very short time.

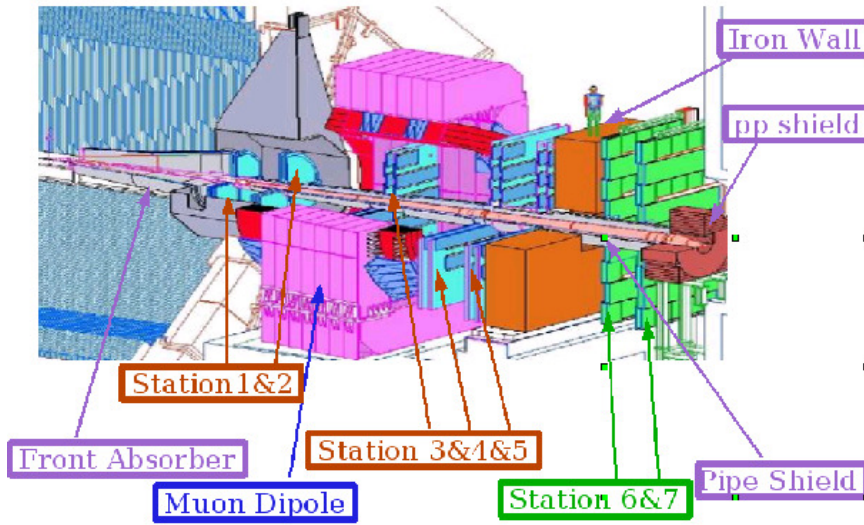


Figure 4.5: The layout of the Muon Spectrometer. Stations 1-5 stands for the tracking system and stations 6-7 show the trigger system [12].

4.2.3 The Tracking System

The Tracking System has two requirements to fulfil. The first requirement is to achieve the spatial resolution of $100\mu\text{m}$. This resolution is necessary to reach the wanted resolution in invariant mass of 100 MeV. The second requirement is to operate in a maximum hit density of about $5 \times 10^{-2}\text{cm}^{-2}$ expected in Pb-Pb collisions. These constraints are fulfilled by the use of Multi-Wire Proportional Chambers (MWPCs) with cathode pad readout. As it is presented in Fig. 4.5, the detectors are segmented in five stations; two are placed in front of the dipole magnet, one is inside and the last two are behind the magnet. Each station is made of two chambers planes, with two cathode planes each, therefore two-dimensional information is provided. Since the hit density decreases with the distance from the beam pipe, larger pads are used at larger radii, as can be seen in Fig. 4.6. To minimize the multiple scattering carbon fibres are used as a material and the thickness of the chamber corresponds to 0.03 of the radiation length. Tracking stations 4 and 5 are shown in Fig. 4.8.

4.2.4 Trigger system

Behind the tracking system an iron muon filter is placed. The filter is 120 cm thick and it decreases the low-energy background particles and it stops hadrons which were not filtered out in the front absorber. Behind this iron filter, the trigger system of the Muon Spectrometer is placed. The system consists of two trigger stations (MT1 and MT2) located 16 meters from the interaction point and 1m apart from each other. Each station is composed of two planes of 18 Resistive Plate Chambers (RPCs). The RPCs are detectors which are made of high resistivity Bakelite electrodes separated by 2mm wide gas gap. The signal is picked up by read-out strips which are placed on both sides, therefore the information provided is bi-dimensional. Finally the output of the trigger electronics is two different thresholds, the Low and High- p_T cuts. It is optimized for the detection of two different resonance families. Cut values of $p_T \cong 1(2)\text{GeV}$ is

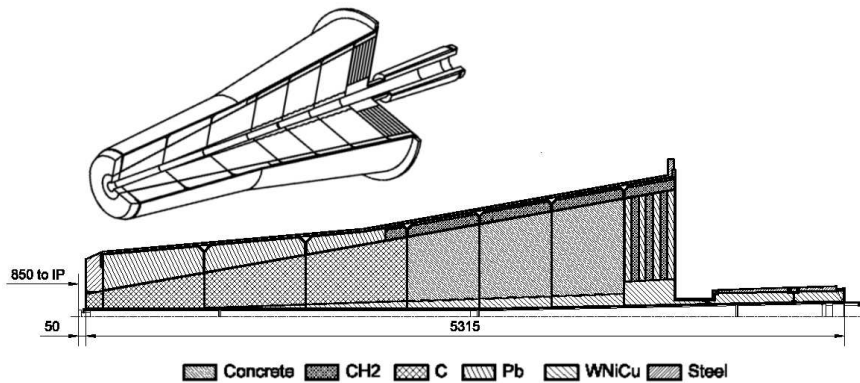


Figure 4.6: Layout of the front absorber of the Muon Spectrometer. Different materials which are used for the absorber are presented [13].

selected for the J/ψ (Υ) detection.

4.3 The Zero Degree Calorimeters (ZDCs)

The Zero Degree Calorimeters (ZDCs) measure the energy of non-interacting nucleons (spectators) from the collision [14]. It is used to measure the multiplicity and then also the centrality of the collision. Therefore it can be used for triggering events with different centralities. In our case it is used to detect emitted neutrons. Since the neutron energy is approximately the same as the beam neutron, the ZDC can be used as a multiplicity detector. The ZDCs consist of two identical sets located at opposite sides of the interaction point. Each set of detectors consists of a neutron (ZN) and proton (ZP) Zero Degree Calorimeter. Since for our purpose measuring neutrons is important, only the ZN will be discussed.

The ZDCs are quartz-fiber spaghetti calorimeters with silica optical fibers as an active material which is embedded in a dense passive material, as an absorber. They are located on both sides at 112.5 meters from the interaction point. The ZN is placed at zero degrees with respect to the beam axis. The principle of the operation is based on the detection of Cherenkov light produced by a charged particle in the quartz fiber. A shower of charged particles is produced by the neutron crossing the passive material. The response is very fast due to the intrinsic speed of the emission process.

The dimensions of the ZN is limited by the space between the two beam pipes which is about 9 cm. Therefore a very dense material, such as W-alloy, is used for the absorber to maximize the shower containment. The quartz fibers are placed 1.6 mm from each other to provide a good uniformity of the response as a function of the impact point and their position is 0° with respect to the incident particle direction of motion. The fibers transport the light right to the photomultipliers (PMTs) and the information from the PMTs provides a corresponding measurement of the shower energy. In Fig. 4.9 the ZN calorimeter can be seen.

The ZN calorimeters have been tested at the CERN SPS with hadron and electron/positron beams. The energy resolution has been measured as a function of $1/\sqrt{E(\text{GeV})}$ and the result can be found in Fig. 4.10. Taken data were fitted and extrapolated to the energy per nucleon in Pb–Pb collisions at LHC, $E = 2.7$ TeV. For the neutrons the

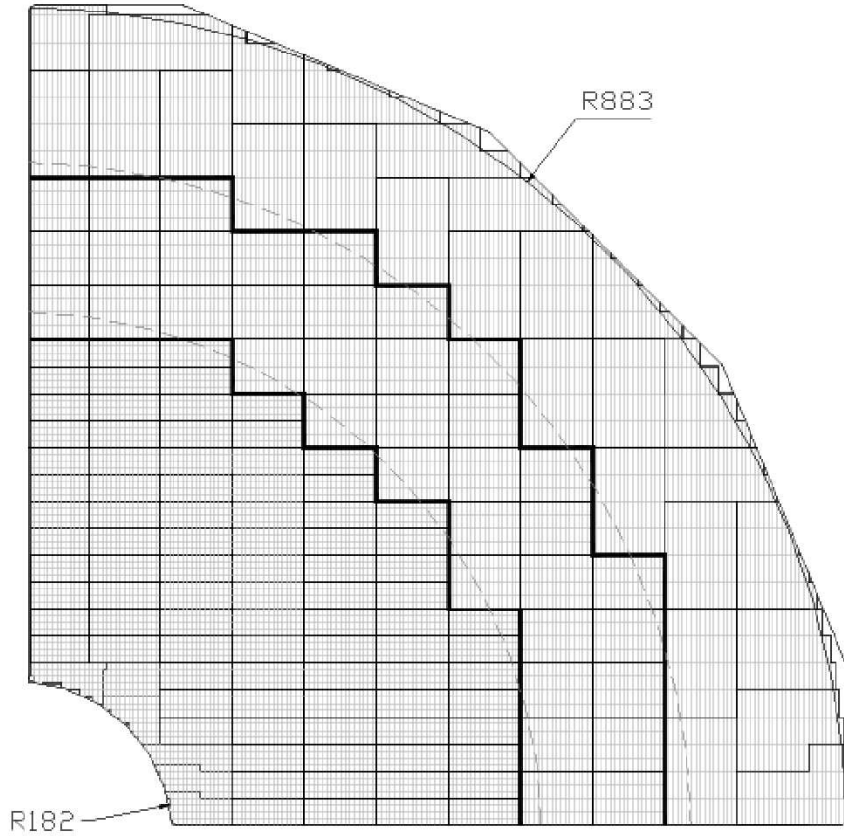


Figure 4.7: The cathode plane layout of Station 1 of the Tracking System of the Muon Spectrometer. Larger pads are used with larger distance from the beam line [13].

energy resolution is about 11.4%, compatible to the spectator energy fluctuations. Furthermore, since the ZN is divided into four tower segmentation, it can be used as a rough position sensitive device. The measurements show that the ZN has good localizing properties and that it can be used to monitor the beam crossing angle at the interaction point and to reconstruct the event plane of the nucleus-nucleus collisions.

4.4 ALICE Diffractive Detector (AD)

The AD detector enhances the efficiency to study diffractive physics and photon induced processes. The system is capable of detecting minimum ionizing particles, therefore less background is expected for UPCs. The system is installed in the forward rapidity region of ALICE [10]. The detectors are made of scintillation plastic pads stations which are located on both sides of the interaction point. One of the two stations is placed on the A side (ADA) at 18 meters from the interaction point and it covers a pseudo-rapidity interval $4.8 < \eta < 6.3$. The second pad station is located on the opposite side (ADC), at 20 meters from the interaction point and it covers the pseudo-rapidity region $-7.0 < \eta < -4.9$.

Each AD detector consists of 8 cells of scintillation plastic of 22×22 cm with

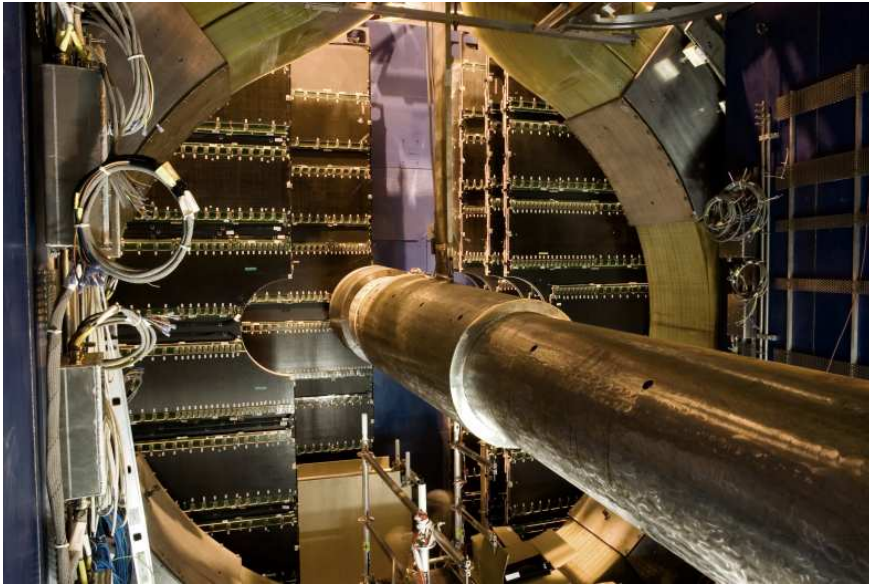


Figure 4.8: Layout of Tracking System Stations 4 and 5 which are located after the dipole magnet of the Muon Spectrometer [13].

thickness of 2.5 cm each. They are arranged around the beam pipe in two layers. The scintillation light is collected by Wave Length Shifters (WLS) which are attached on two sides of each cell. The WLS transfer the collected scintillation light to optical fibres where it is guided to Photomultiplier (PMT) and converted into an electric signal. A prototype of the AD detector can be seen in Fig. 4.11.

4.5 VZERO detector

The VZERO is a scintillation detector designed to detect particles in the forward region of the collision [28]. The main function of this detector is triggering, but it can also be used to monitor the LHC beam conditions, to reject beam-induced background and to measure basic physics quantities. For our purposes the VZERO is used as a trigger of events for which the VZERO detector is empty.

Two VZERO arrays are located on both sides of the interaction point, VZERO-A and VZERO-C which cover the pseudo-rapidity ranges of $2.8 < \eta < 5.1$ and $-3.7 < \eta < -1.7$. VZERO-A is placed at a distance of 239 centimeters from the interaction point and the VZERO-C is fixed on the front face of the hadronic absorber, 90 centimeters from the interaction point.

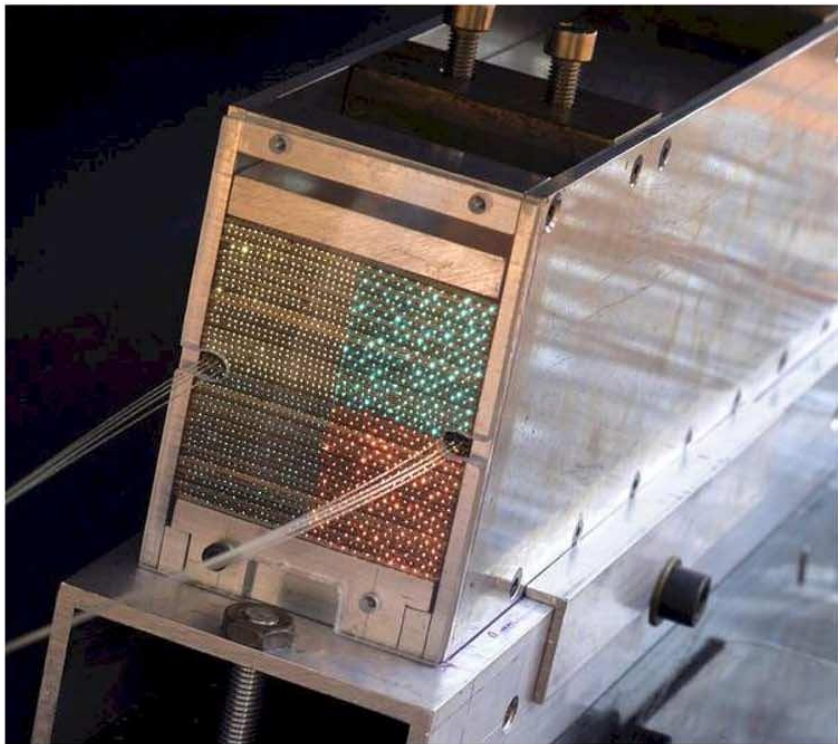


Figure 4.9: A photograph of the Zero Degree Neutron Calorimeter [14].

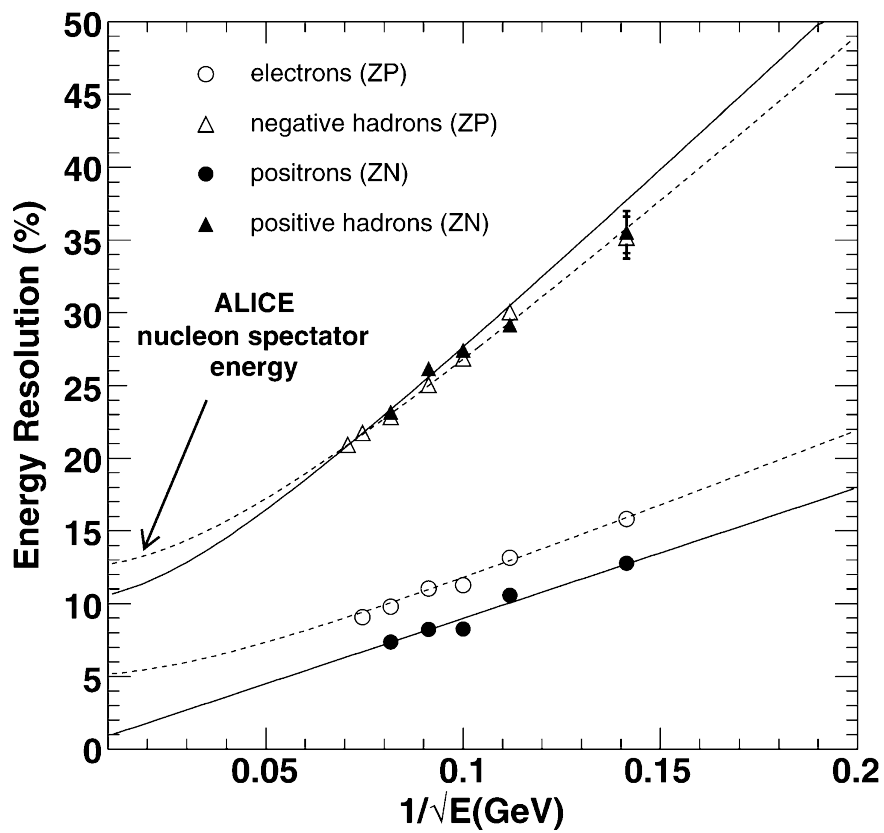


Figure 4.10: The energy resolution of Zero Degree Calorimeter measured for hadron and electron beams. It is measured in dependence on $1/\sqrt{E}(\text{GeV})$ [14].

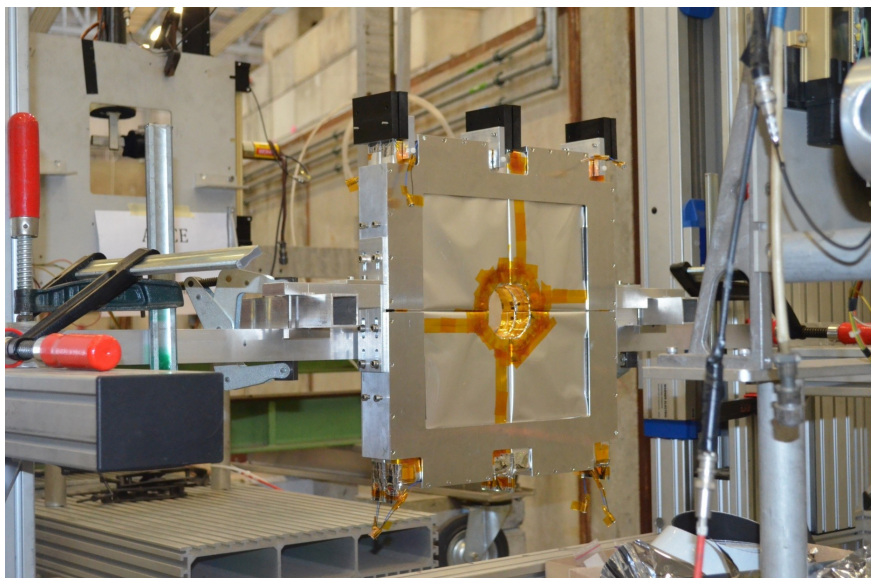


Figure 4.11: The final prototype of the ALICE Diffractive detector [10].

Chapter 5

Previous measurements

In this chapter I am going to summarize three measurements of coherently photoproduced J/ψ in UPCs. The first two are from ALICE and the third one is from CMS.

5.1 Coherent J/ψ photoproduction in ultra-peripheral Pb–Pb collisions at $\sqrt{s_{NN}} = 2.76\text{TeV}$ [1]

The ALICE collaboration reported the very first measurement at the LHC of coherent J/ψ photoproduction in Pb–Pb UPCs at $\sqrt{s_{NN}} = 2.76\text{ TeV}$. The J/ψ was measured in the dimuon decay channel in the forward rapidity region $-3.6 < y < -2.6$. As it was said before, the experimental definition of a coherently produced J/ψ meson depends on its p_T . Coherent candidates were obtained by selecting two muons with transverse momentum $p_T < 0.3\text{ GeV}$.

5.1.1 Data selection

The analysis is based on a sample of events collected during the Pb–Pb run 2011. The data was selected with a special trigger FUPC which selects UPC events in which a dimuon pair is produced. The integrated luminosity corresponded to about $55\mu\text{b}^{-1}$.

The FUPC trigger selected events with two muons from either photon-photon production ($\gamma\gamma \rightarrow \mu^+\mu^-$) or from J/ψ decay and it selected 3.16×10^6 events and it requires:

- A single muon trigger above a 1 GeV p_T -threshold.
- At least one hit in the VZERO-C detector, also VZERO-C rejects the remaining beam-gas events
- No hits in the VZERO-A detector to avoid hadronic collisions.

The following offline event selection criteria were applied:

- Two reconstructed tracks in the muon arm.
- Cut on the product $p \times \text{DCA}$ at 6 times the standard deviation of the dispersion.
- At least one of the muon candidates are required to match a trigger track above 1 GeV p_T -threshold

- Both tracks have pseudorapidities in the range $-3.7 < |\eta_{1,2}| < -2.5$.
- The tracks leave the absorber in the range $17.5 < R_{abs} < 89.5$ cm.
- Dimuon rapidity is in the range $-3.6 < y < -2.6$.
- Two tracks with opposite charges.
- Energy deposit in the ZDC detector is below 6 TeV on each side.
- Dimuons have $p_T < 0.3$ GeV and the invariant mass $2.6 < M_{inv} < 3.4$ GeV.
- VZERO-C offline timing, if available, is compatible with crossing beams.

After the FUPC trigger and offline event selection a sample of 117 events was used for the analysis.

The acceptance and efficiency of J/ψ reconstruction were calculated using a sample of J/ψ events generated by STARLIGHT [29]. The sample was folded with the detector Monte Carlo simulation. The product of the acceptance and efficiency correction $(A \times \varepsilon)_{J/\psi}$ was calculated as the ratio of the number of simulated events to the number of generated events in the rapidity range $-3.6 < y < -2.6$. The results for the acceptance and efficiency was found to be 16.6% for coherent J/ψ and 14.3% for incoherent J/ψ and the relative systematic uncertainty on the $(A \times \varepsilon)_{J/\psi}$ correction was 6%.

5.1.2 Results

The invariant mass distribution for muon pairs ($\mu^+\mu^-$) with a range $2.2 < M_{inv} < 4.6$ GeV/ c^2 is shown in Fig. 5.1. The red curve represents the continuum of $\gamma + \gamma \rightarrow \mu^+\mu^-$ and the black curve is the fit with a Crystal Ball function to extract the J/ψ signal. The central mass value of the fit is 3.123 ± 0.011 GeV which is within 2.4σ of the well known mass of J/ψ . The number of all J/ψ candidates extracted from the fit is $N_{yield} = 96 \pm 12(\text{stat}) \pm 6(\text{syst})$.

To obtain the number of coherently photoproduced J/ψ candidates, the fraction f_D of the J/ψ mesons coming from feed-down had to be estimated. The fraction comes from the decay $\Psi' \rightarrow J/\psi + \text{anything}$ and it is estimated by simulating a sample of coherently produced Ψ' mesons with STARLIGHT. The J/ψ fraction coming from the decay Ψ' is given:

$$f_D^P = \frac{\sigma_{\Psi'} BR(\Psi' \rightarrow J/\psi + \text{anything})(A \times \varepsilon)_{\Psi' \rightarrow J/\psi}^P}{\sigma_{J/\psi}(A \times \varepsilon)_{J/\psi}}, \quad (5.1)$$

where the P stands for different polarizations of the produced J/ψ , such as no polarization (NP), full transverse (T) and full longitudinal (L) polarization. The cross sections were computed for $p_T < 0.3$ GeV. The best estimate of all polarizations was taken and the fraction $f_D = (11 \pm 6\%)$.

The p_T distribution for dimuon candidates is shown in Fig. 5.2. The clear peak at low p_T is mainly due to coherent J/ψ events and the tail comes from incoherently produced J/ψ mesons. Nevertheless in region $p_T < 0.3$ GeV are some incoherent J/ψ produced. Using the ratio $\sigma_{inc}/\sigma_{coh}$ and $(A \times \varepsilon)$ the fraction of incoherent to coherent events was calculated to be $f_I = 0.12$. The contamination from hadronic production in the sample is low to about 1%, therefore a correction is not needed.

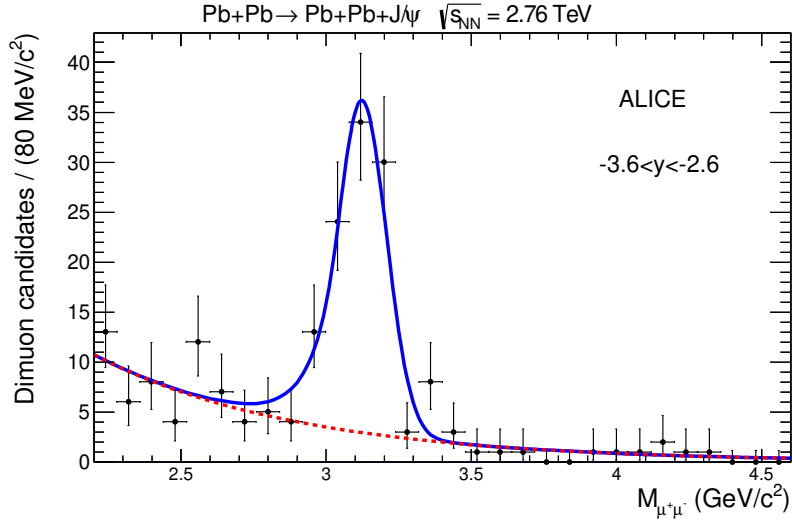


Figure 5.1: Invariant mass distribution for events with two oppositely charged muons in the rapidity range $-3.6 < y < -2.6$ [1].

Finally, the number of coherent J/ψ mesons is obtained from:

$$N_{J/\psi}^{\text{coh}} = \frac{N_{\text{yield}}}{1 + f_D + f_I} \quad (5.2)$$

with the result of number of coherent J/ψ candidates:

$$N_{J/\psi}^{\text{coh}} = 78 \pm 10(\text{stat})_{-11}^{+7}(\text{syst}).$$

The differential cross section of coherently photoproduced J/ψ is given by:

$$\frac{d\sigma_{J/\psi}^{\text{coh}}}{dy} = \frac{N_{J/\psi}^{\text{coh}}}{\mathcal{B}(J/\psi \rightarrow \mu^+\mu^-) \mathcal{L}_{\text{int}} \Delta y (A \times \varepsilon)_{J/\psi} \varepsilon_{\text{trig}}} \quad (5.3)$$

where $(A \times \varepsilon)_{J/\psi}$ corresponds to the acceptance and efficiency of the muon spectrometer detector, $\varepsilon_{\text{trig}}$ is the VZERO trigger efficiency, $\mathcal{B}(J/\psi \rightarrow \mu^+\mu^-) = 5.93\%$ is the branching ratio, $\Delta y = 1$ is the rapidity interval bin and \mathcal{L}_{int} is the integrated luminosity. The final cross section was measured to be:

$$\frac{d\sigma_{J/\psi}^{\text{coh}}}{dy} = 1.00 \pm 0.18(\text{stat})_{-0.26}^{+0.24}(\text{syst}) \text{ mb}$$

As it was said earlier, the measurement is sensitive to gluon shadowing. In this rapidity region $-3.6 < y < -2.6$, the shadowing is reduced compared with shadowing in mid-rapidity. For instance, at rapidity $y = 3$ the center-of-mass energy of the produced J/ψ corresponds to either $W_{\gamma p} = 414$ GeV or $W_{\gamma p} = 21$ GeV. According to interactions simulated with STARLIGHT, interactions with $W_{\gamma p} = 21$ GeV contribute to the cross section with 94% and the other contribution only with 6%. Therefore, the total cross section at $y = 3$ is mainly sensitive to the gluon distribution around $x = 2 \times 10^{-2}$.

The measured coherent cross section $\frac{d\sigma_{J/\psi}^{\text{coh}}}{dy} = 1.00 \pm 0.18(\text{stat})_{-0.26}^{+0.24}(\text{syst}) \text{ mb}$ is shown in Fig. 5.3 and it is compared to model predictions. To have a better look at the deviations of the models, in Fig. 5.4 the cross section integrated over the rapidity range is shown. Models, that are in the best agreement with the measurement,

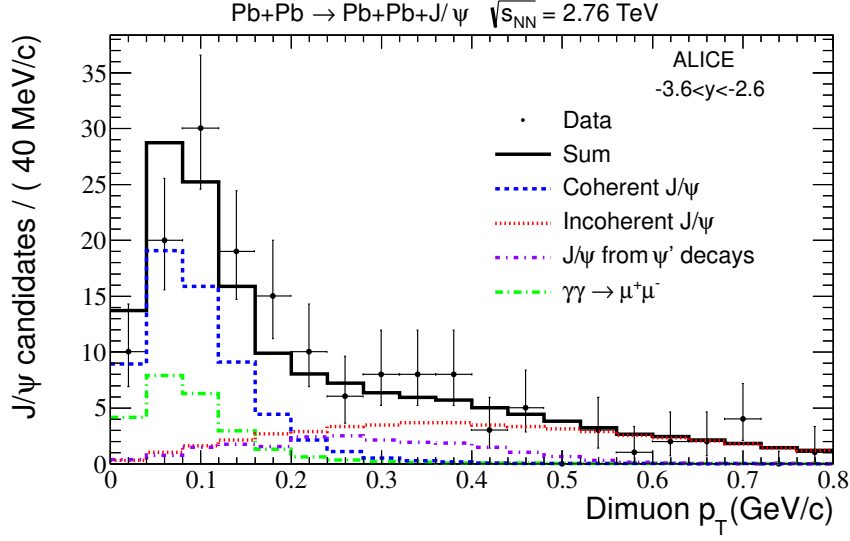


Figure 5.2: Dimuon p_T distribution. The data is fitted summing four different Monte Carlo templates [1].

are RSZ-LTA, AB-EPS09 and AB-EPS08. All these models include moderate nuclear gluon shadowing. On the other hand, the largest deviations have models STARLIGHT and AB-MSTW08.

5.2 Coherent J/ψ photoproduction at forward rapidity in ultra-peripheral Pb–Pb collisions at $\sqrt{s_{NN}} = 5.02$ TeV [2]

The analysis presented in this paper is based on a data sample from 2015 and 2018 data taking periods at $\sqrt{s_{NN}} = 5.02$ TeV. These two periods are characterized by similar conditions and detector performance. Two oppositely charged tracks in the muon spectrometer and vetoes on V0A, ADA and ADC beam-beam interactions were required by the trigger. Muons with transverse momentum $p_T = 1$ GeV were triggered. The estimated luminosities for 2015 and 2018 were $216\mu\text{b}^{-1}$ and $538\mu\text{b}^{-1}$ respectively. The selection of events included: only two tracks with opposite electric charge in the muon spectrometer, the pseudorapidity of each track in the range $-4.0 < \eta < -2.5$ and the requirements for tracks same as in [1]. For exclusively produced J/ψ at most two fired cells in V0C are required in an otherwise empty detector. The coherent J/ψ candidates were obtained by selecting muons with transverse momentum $p_T < 0.25$ GeV.

The hadronic pile-up probability was lower than 0.2%. However from the electromagnetic pair production process $\gamma\gamma \rightarrow e^+e^-$ the pile-up was more significant in sub-detectors V0A, V0C, ADA, ADC and SPD vetoes. The probability of veto rejection was determined in these sub-detectors. The veto inefficiency of V0A was found to be $p_{V0A} = 4.6 \pm 0.2\%$ and in ADA and ADC it was found to be about 0.2%. The average veto efficiency was calculated as $\epsilon_{veto} = (1 - p_{V0A})(1 - p_{ADA})(1 - p_{ADC}) = 95.0\%$. If the SPD veto is used then the efficiency was calculated to be $\epsilon_{veto} = 86.0\%$. The

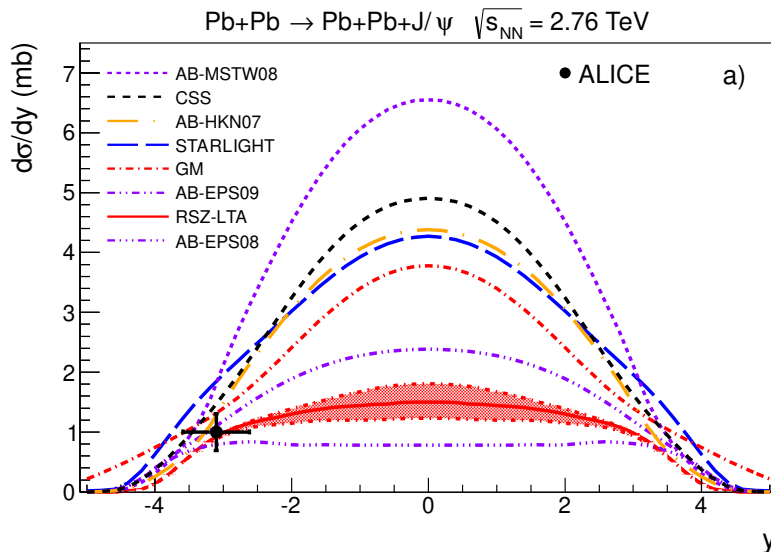


Figure 5.3: The differential cross section of coherently produced J/ψ at rapidity interval $-3.6 < y < -2.6$ which is shown by the vertical bar of the measurement point. The error is quadratic sum of the statistical and systematic errors. With the colored curves different theoretical predictions are shown [1].

acceptance and efficiency of J/ψ and ψ' was evaluated using a larger data sample generated by STARLIGHT, the acceptance and efficiency of feed-down $\Psi' \rightarrow J/\psi + \pi\pi$ were obtained from the STARLIGHT generator. It was assumed that the transverse polarization of Ψ' comes in the feed-down J/ψ .

5.2.1 Results

The invariant mass distribution for selected unlike-sign muon pairs in the rapidity range $-4.0 < y < -2.5$ is shown in Fig 5.5. The invariant masses of coherently photoproduced J/ψ and Ψ' are fitted by Crystal Ball functions. The background is fitted by the template of events corresponding to the process $\gamma\gamma \rightarrow \mu^+\mu^-$ made in STARLIGHT. The fourth-order polynomial is used to parameterize the result and it smoothly turns into an exponential tail as from $4 \text{ GeV}/c^2$. The fitted curve agrees within 2.5 standard deviations with the value received from the generated data set.

The number of produced J/ψ $N(J/\psi) = 21\,746 \pm 190$ corresponds to the raw inclusive J/ψ yield and it contains both coherent and incoherent J/ψ photoproduction. The number was obtained by fitting the invariant mass spectrum in the range $2.2 < m_{\mu\mu} < 6 \text{ GeV}/c^2$ by the Crystal Ball functions. The invariant mass obtained from the fit was $m_{J/\psi} = 3.0993 \pm 0.0009 \text{ GeV}/c^2$, which is in good agreement with the PDG value within 3 standard deviations. The raw inclusive Ψ' yield $N(\Psi')$ is also obtained from the mass fit, however the mass of Ψ' is fixed due to the small statistics.

Coherent and incoherent photoproduction are separated studying the transverse momentum p_T . The p_T distribution of the dimuon pair with $2.85 < m_{\mu\mu} < 3.35 \text{ GeV}/c^2$ is shown in Fig. 5.6 in the rapidity interval $-4.0 < y < 2.5$, also different rapidity sub-ranges were measured and are collected in Fig. 5.7. The distributions are fitted by data

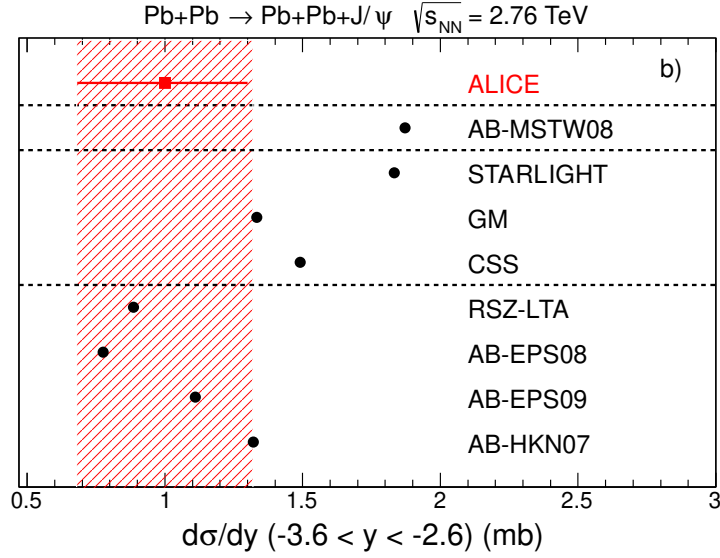


Figure 5.4: The cross section integrated over the rapidity range $-3.6 < y < -2.6$ compared to the theoretical models [1].

generated by STARLIGHT. The data templates correspond to various production mechanisms, which contribute to the final template, such as: coherent and incoherent J/ ψ production, feed-down J/ ψ from coherent and incoherent Ψ' decays and continuum dimuons from $\gamma\gamma$ interactions. All these fits are shown in the figure with different line colors.

The extracted incoherent J/ ψ fraction for $p_T < 0.25$ GeV/c can be determined as

$$f_I = \frac{N(\text{incoherent J}/\psi)}{N(\text{coherent J}/\psi)}. \quad (5.4)$$

It depends on the rapidity interval and it goes from 3.2% to 6.1%, see Tab. 5.1.

The incoherent J/ ψ photoproduction accompanied by nucleon dissociation was considered in the fits for a better description of the tail formed at high- p_T . The data set provided by the H1 collaboration measurements of the dissociative J/ ψ photoproduction were used to get the fitting equation:

$$\frac{dN}{dp_T} \sim p_T \left(1 + \frac{b_{pd}}{n_{pd}} p_T^2\right)^{-n_{pd}}, \quad (5.5)$$

where the fit parameters are obtained from H1 measurements with different photon-proton center-of-mass energy intervals.

The ratio of raw inclusive Ψ' and J/ ψ yields is extracted from the fits of the invariant mass of $\mu^+\mu^-$ pairs described above denoting:

$$R_N = \frac{N(\Psi')}{N(\text{J}/\psi)} = 0.025 \pm 0.003(\text{stat.}) \pm 0.0035(\text{syst.}), \quad (5.6)$$

the ratio can also be expressed in terms of the primary coherent photoproduction cross

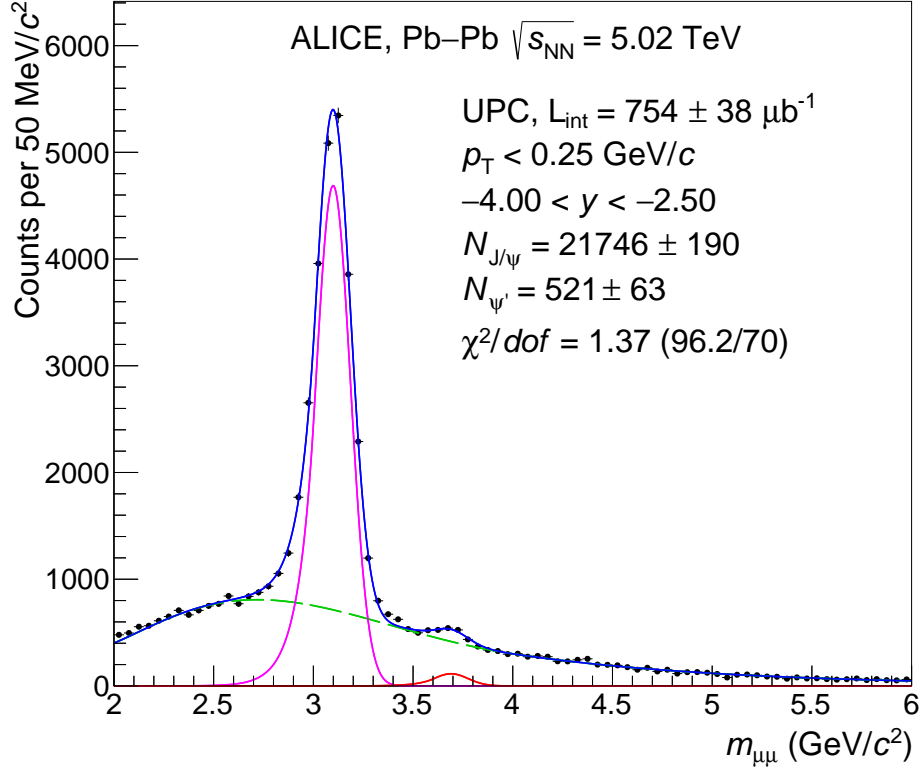


Figure 5.5: Invariant mass distribution for muon pairs. The pink and red lines correspond to Crystall Ball functions representing J/ψ and Ψ' signals. The dashed green line corresponds to the background and the solid blue line corresponds to the sum of background and signal functions [2].

section $\sigma(\Psi')$ and $\sigma(J/\psi)$

$$R_N = \frac{\sigma(\Psi')BR(\Psi' \rightarrow \mu\mu)\varepsilon(\Psi')}{\sigma(J/\psi)BR(J/\psi \rightarrow \mu\mu)\varepsilon(J/\psi) + \sigma(\Psi')BR(\Psi' \rightarrow J/\psi)\varepsilon(\Psi' \rightarrow J/\psi)BR(J/\psi \rightarrow \mu\mu)}, \quad (5.7)$$

where $\varepsilon(J/\psi) = 12.0\%$, $\varepsilon(\Psi') = 15.8\%$ and $\varepsilon(\Psi' \rightarrow J/\psi) = 7.2\%$ are the efficiency corrections for primary coherent J/ψ , Ψ' and feed-down J/ψ from coherent Ψ' decays estimated with STARLIGHT, while $BR(J/\psi \rightarrow \mu\mu) = (5.961 \pm 0.033)\%$, $BR(\Psi' \rightarrow \mu\mu) = (0.80 \pm 0.06)\%$, $BR(\Psi' \rightarrow J/\psi + \text{anything}) = (61.4 \pm 0.6)\%$ are the corresponding branching ratios. Eq. 5.7 and the measured R_N value were used to extract the ratio of primary coherent Ψ' and J/ψ photoproduction cross sections:

$$R = \frac{\sigma(\Psi')}{\sigma(J/\psi)} = 0.150 \pm 0.018(\text{stat.}) \pm 0.021(\text{syst.}) \pm 0.007(\text{BR}). \quad (5.8)$$

The measured ratio of the cross sections is in good agreement with data from H1 ep measurements ($R \approx 0.166$) and with LHCb pp experiments ($R \approx 0.19$). The value of R also satisfies the Leading Twist Approximation predictions, which spreads from 0.13 to 0.18. ALICE measured coherent Ψ' - J/ψ cross section ratio at central rapidity Pb-Pb UPCs at $\sqrt{s_{NN}} = 2.76\text{TeV}$ to be $0.34^{+0.08}_{-0.07}$. The value is more than doubled, but

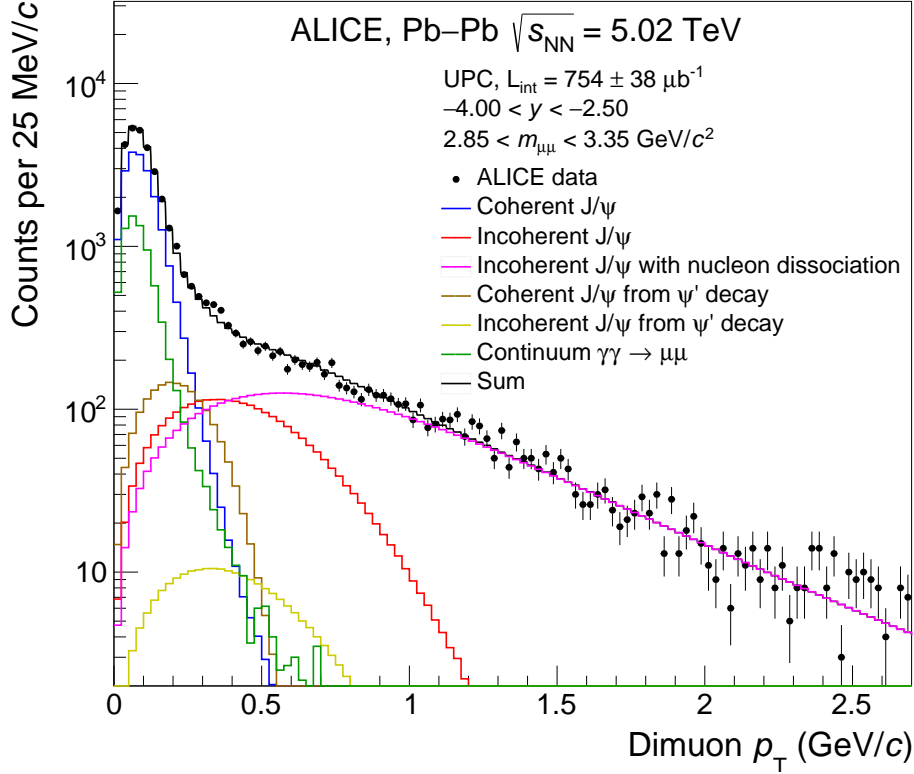


Figure 5.6: Transverse momentum distribution for muon pairs in range $2.85 < m_{\mu\mu} < 3.35 \text{ GeV}/c^2$ [2].

it is still within 2.5 standard deviations. The fraction of feed-down J/ψ from Ψ' and primary J/ψ yield is given by:

$$f_D = \frac{N(\text{feed-down } J/\psi)}{N(\text{primary } J/\psi)} = R \frac{\varepsilon(\Psi' \rightarrow J/\psi)}{\varepsilon(J/\psi)} BR(\Psi' \rightarrow J/\psi) \quad (5.9)$$

For transverse momentum cut $p_T < 0.25 \text{ GeV}/c$ one gets $f_D = 5.5\% \pm 1.0\%$.

The coherent J/ψ differential cross section follows:

$$\frac{d\sigma_{J/\psi}^{\text{coh}}}{dy} = \frac{N(J/\psi)}{(1 + f_I + f_D)\varepsilon(J/\psi)BR(J/\psi \rightarrow \mu\mu)\varepsilon_{\text{veto}}L_{\text{int}}\Delta y}, \quad (5.10)$$

where $N(J/\psi)$ is the J/ψ yield extracted from the invariant mass fit, $(1 + f_I + f_D)$ correspond to the incoherent and feed-down fractions, $\varepsilon_{\text{veto}}$ is the veto efficiency, L_{int} is the integrated luminosity and Δy is the rapidity bin. All calculated values of the J/ψ yields, fractions f_I , f_D , the efficiency and cross sections are summarized in Tab. 5.1 for different rapidity intervals. The systematic uncertainties are determined from the composition of several different sources which were largely studied in the paper.

The measured differential cross section of coherently photoproduced J/ψ is shown in Fig. 5.8. It is plotted in dependence of the rapidity range $-4.0 < y < -2.5$ and it is compared with several models. The EPS09 leading order model was discussed in Chapter 3. The covered rapidity ranges correspond to a Bjorken- x of $x \in (1.1 \cdot$

rapidity range	$N_{J/\psi}$	ε	f_D	f_I	$d\sigma_{J/\psi}^{\text{coh}}/dy$ (mb)
(-4.00, -2.50)	21747 ± 190	0.120	0.055	0.055	2.549 ± 0.022 (stat.) $^{+0.209}_{-0.237}$ (syst.)
(-4.00, -3.75)	974 ± 36	0.051	0.055	0.060	1.621 ± 0.061 (stat.) $^{+0.135}_{-0.148}$ (syst.)
(-3.75, -3.50)	3217 ± 70	0.140	0.055	0.059	1.936 ± 0.042 (stat.) $^{+0.166}_{-0.190}$ (syst.)
(-3.50, -3.25)	5769 ± 98	0.204	0.055	0.061	2.376 ± 0.040 (stat.) $^{+0.212}_{-0.229}$ (syst.)
(-3.25, -3.00)	6387 ± 105	0.191	0.055	0.052	2.830 ± 0.047 (stat.) $^{+0.253}_{-0.280}$ (syst.)
(-3.00, -2.75)	4229 ± 85	0.119	0.055	0.051	3.014 ± 0.061 (stat.) $^{+0.259}_{-0.294}$ (syst.)
(-2.75, -2.50)	1190 ± 47	0.029	0.054	0.032	3.585 ± 0.141 (stat.) $^{+0.298}_{-0.368}$ (syst.)

Table 5.1: J/ψ yields, efficiencies, f_I and f_D fractions and coherent J/ψ cross sections [2].

10^{-5} ; $5.1 \cdot 10^{-5}$) or $x \in (0.7 \cdot 10^{-2}; 3.3 \cdot 10^{-2})$ in dependence on which nucleus is the emitter of the photon and which one is the target. The nuclear shadowing dominates for gluon of high Bjorken- x ($x \approx 10^{-2}$) at forward rapidities. The measured cross section was compared with the Impulse Approximation, giving the result of the factor of shadowing to range from $\approx 60\%$ at $y = -2.5$ to $\approx 95\%$ at $y = -4.0$, where it was assumed that the contribution from low Bjorken- x ($x \approx 10^{-5}$) is negligible. The cross section in the full rapidity range was determined to be $\frac{d\sigma_{J/\psi}^{\text{coh}}}{dy} = 2.549 \pm 0.022$ (stat.) $^{+0.209}_{-0.237}$ (syst.).

5.3 Coherent J/ψ photoproduction on ultra-peripheral Pb-Pb collisions at $\sqrt{s_{NN}} = 2.76$ with the CMS experiment [3]

The CMS collaboration reported the study of the coherent J/ψ photoproduction cross section with associated production of forward or backward neutrons measured in UPCs at $\sqrt{s_{NN}} = 2.76$ TeV. This associated neutron production is called neutron break-up mode. The UPC trigger selected events with one or more neutrons detected by the zero degree calorimeters (ZDCs) in the forward or backward direction from the interaction point. The J/ψ candidates are reconstructed through the dimuon decay channel in the rapidity interval $1.8 < |y| < 2.3$.

5.3.1 Data selection

The data sample was collected with the CMS detector in the 2011 PbPb run with integrated luminosity of $159 \mu b^{-1}$. The UPC trigger is used to select data from both coherent and incoherent J/ψ mesons and $\gamma + \gamma \rightarrow \mu^+ \mu^-$ events and it has the following requirements:

- An energy deposit consistent with at least one neutron in either of the ZDCs.
- No activity in at least one of the BSC+ or BSC- scintillators.
- The presence of at least one single muon without a p_T threshold requirement, and at least one track in the pixel detector.

To suppress the beam-gas interactions and non-UPC events additional offline requirements were applied:

- The z position of the primary vertex is required to be within 25 cm of the beam spot center.
- The length of the pixel cluster must be consistent with tracks originating from this vertex to remove beam-background events that produce elongated pixel cluster.
- Rejection of events which have time difference between two hits from BSCs above 20 ns to remove beam-halo events.

The presence of at least one neutron is required by the UPC trigger. The events are classified by the pattern of neutron deposition energy measured in ZDCs. The energy spectrum shows a clear one neutron peak with a resolution of about 20%. The energy resolution is good enough to separate between event with zero (less than 420 GeV deposit in ZDC), one (420 GeV – 1600 GeV deposit) or multiple (more than 1600 GeV) neutrons detected in ZDCs. The UPC trigger selects break-up modes:

(XnXn) - at least one neutron detected in both forward and backward direction.

(Xn0n) - at least one neutron on one side of the interaction point - the case from which the coherent J/ψ cross section is measured.

(1n0n) - exactly one neutron on one side.

(1n1n) - exactly one neutron on both sides of the interaction point.

To reject the non-UPC events two selection criteria are additionally applied:

- Only events with exactly two reconstructed tracks are kept.
- The HF cell with the highest energy deposit is required to have energy below 3.5 GeV.

As it was said the J/ψ candidates are reconstructed through the dimuon channel. Both muons have to pass these criteria. They must be in pseudorapidity region $1.2 < |\eta| < 2.4$ and p_T region $1.2 < p_T < 1.8$ GeV. The single muons are required to satisfy following criteria:

- More than 4 hits in the tracker, at least one of which is required to be in a pixel layer.
- A track fit with a χ^2 per degree of freedom less than three.
- A transverse (longitudinal) impact parameter less than 0.3 (20) cm from the measured vertex.

Only events with dimuons having $p_T < 1.0$ GeV and rapidity $1.8 < |y| < 2.3$ were used. The invariant mass region $2.6 < m(\mu^+\mu^-) < 3.5$ GeV for dimuon candidates was required. No like-sign muon pairs were found in this region.

To calculate the acceptance and efficiency corrections for signal extraction the data generated by the Monte Carlo STARLIGHT generator was used. All the events were processed with the full CMS simulation and reconstruction software.

5.3.2 Results

After all the selections, dimuon invariant mass and p_T distribution are fitted. The dimuon invariant mass distribution is shown in Fig. 5.9. The sum of coherent and incoherent J/ψ is described with a Crystal Ball function, it counts with the detector resolution and the radiative tail from internal bremsstrahlung. The green second-order polynomial curve represents the $\gamma + \gamma \rightarrow \mu^+ \mu^-$ events. The fit constraints the number of coherent, incoherent J/ψ and dimuon continuum events to be the same as in the p_T distribution that is shown in Fig. 5.10. The black curve represents the sum of the coherent, incoherent J/ψ and $\gamma + \gamma$. The red, blue and green curves represent coherent, incoherent and $\gamma + \gamma$ events separately. For $p_T < 0.15$ GeV coherently produced J/ψ dominates, whereas incoherent J/ψ events are dominant for $p_T > 0.15$ GeV. For events with $p_T < 0.15$ GeV in rapidity interval $1.8 < |y| < 2.3$, the fit yields 207 ± 18 (stat) for coherent J/ψ candidates, 75 ± 13 (stat) for incoherent J/ψ and 75 ± 13 (stat) for $\gamma + \gamma$ events.

In addition, two cases were studied using the data sample:

- Neutrons are emitted in the same rapidity hemisphere as the J/ψ .
- Neutrons are emitted in the opposite rapidity hemisphere than the J/ψ .

The number of coherently produced J/ψ mesons was found to be consistent between these two cases (within the statistical and systematic uncertainties). It implies that the J/ψ photoproduction and the emission of neutrons are independent processes. For the incoherent J/ψ events it was found that most of the events were in the configuration with photoproduced J/ψ and emitted neutrons in the same hemisphere. It is in agreement with photoproduced J/ψ analysis of protons measured by ALICE and reported here [30]. This observation suggest that two contributions of low- x and high- x in cross section are decoupled and can be more easily observed then in coherent J/ψ events. Because the sample of data is small, both configurations are summed and used to measure coherent J/ψ cross section.

The coherent J/ψ cross section for the $(Xn0n)$ break-up mode is given by:

$$\frac{\sigma_{(Xn0n)}^{\text{coh}}}{y}(J/\psi) = \frac{N_{(Xn0n)}^{\text{coh}}}{\mathcal{B}(J/\psi \rightarrow \mu^+ \mu^-) \mathcal{L}_{\text{int}} \Delta y (A \epsilon)^{J/\psi}} \quad (5.11)$$

where $\mathcal{B}(J/\psi \rightarrow \mu^+ \mu^-) = 5.96 \pm 0.03(\text{syst.})\%$ is the branching ratio of J/ψ decay to dimuons, $N_{(Xn0n)}^{\text{coh}}$ is the coherent J/ψ yield of prompt J/ψ candidates for $p_T < 0.15$ GeV, $\mathcal{L}_{\text{int}} = 159 \pm 8(\text{syst.}) \mu\text{b}^{-1}$ is the integrated luminosity, $\Delta y = 1$ is the rapidity bin width and $(A \epsilon)^{J/\psi} = 5.9 \pm 0.5(\text{stat.}) \%$ is the combined acceptance times efficiency correction factor. The coherent J/ψ yield of prompt J/ψ candidates is given by:

$$N_{(Xn0n)}^{\text{coh}} = \frac{N_{\text{yield}}}{1 + f_D} \quad (5.12)$$

where $N_{\text{yield}} = 207 \pm 18(\text{stat.})$ is extracted from Fig. 5.10 and f_D is the fraction of J/ψ mesons coming from coherent $\Psi(2S) \rightarrow J/\psi + \text{anything}$. This $f_D = 0.018 \pm 18(\text{stat.})$ correction is obtained from STARLIGHT generated data. Thus, the cross section of coherently photoproduced J/ψ in $(Xn0n)$ break-up mode is

$$\frac{\sigma_{(Xn0n)}^{\text{coh}}}{y(J/\psi)} = 0.36 \pm 0.04(\text{stat.}) \pm 0.04\text{mb.}$$

To obtain the total coherent J/ψ photoproduction cross section, this result needs to be corrected by the scaling factor between the $(X_n 0_n)$ break-up mode and the total cross section which is $5.1 \pm 0.5(\text{theo.})$. After applying this scaling factor, the obtained total cross section of coherently photoproduced J/ψ is:

$$\frac{\sigma_{(X_n 0_n)}^{\text{coh}}}{y(J/\psi)} = 1.82 \pm 0.22(\text{stat.}) \pm 0.20(\text{syst.}) \pm 0.19(\text{theo.})\text{mb.}$$

The measured coherent J/ψ cross section is compared to results from ALICE (mentioned earlier) in Fig. 5.11. It is compared to the impulse approximation and to the results of leading twist approximation. The leading twist approximation is in good agreement with measured data and it is obtained from [31]. The theoretical uncertainty for the leading twist approximation is 12% and is due to the uncertainty in the strength of the gluon recombination mechanism. The impulse approximation uses data from exclusive J/ψ production in $\gamma + p$ interaction to estimate the coherent J/ψ cross section in $\gamma + Pb$ collisions and it neglects all nuclear effects such as the expected modifications of the gluon density in the lead nuclei compared to that of the proton. As we can see this approximation overpredicts the CMS data by more than 3 standard deviations in the rapidity interval.

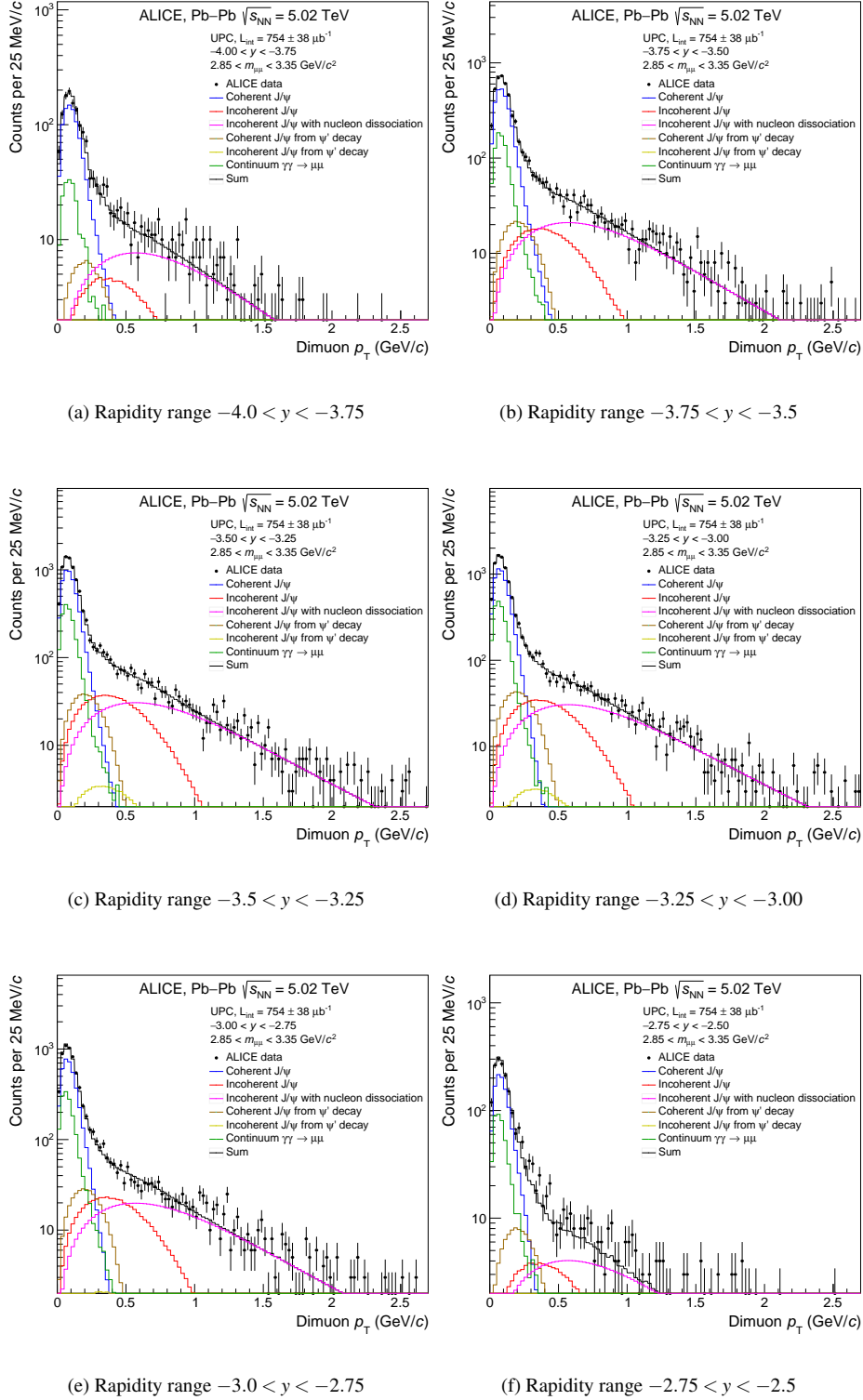


Figure 5.7: The p_T distributions for different rapidity intervals for dimuons in the range $2.85 < m_{\mu\mu} < 3.35 \text{ GeV}/c^2$ [2].

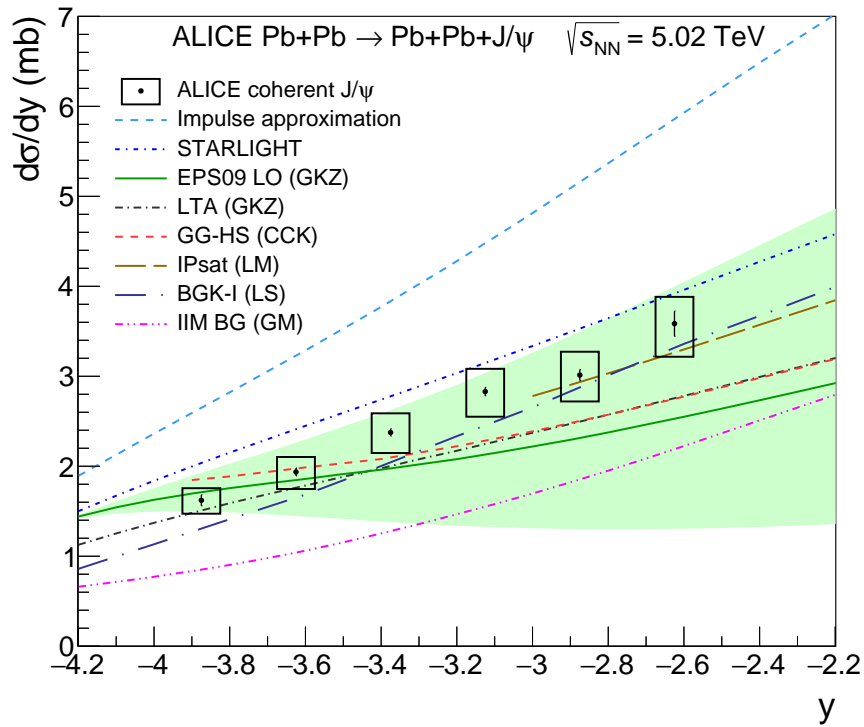


Figure 5.8: Measured coherent differential cross section of photoproduced J/ ψ in ultra-peripheral collisions at $\sqrt{s_{NN}} = 5.02$ TeV. The statistical uncertainties are represented by the error bars and the boxes around the points are the systematic errors. The colored lines represent different theoretical calculations and the green band represents the uncertainties of the EPS09 LO model discussed in Chapter 3 [2].

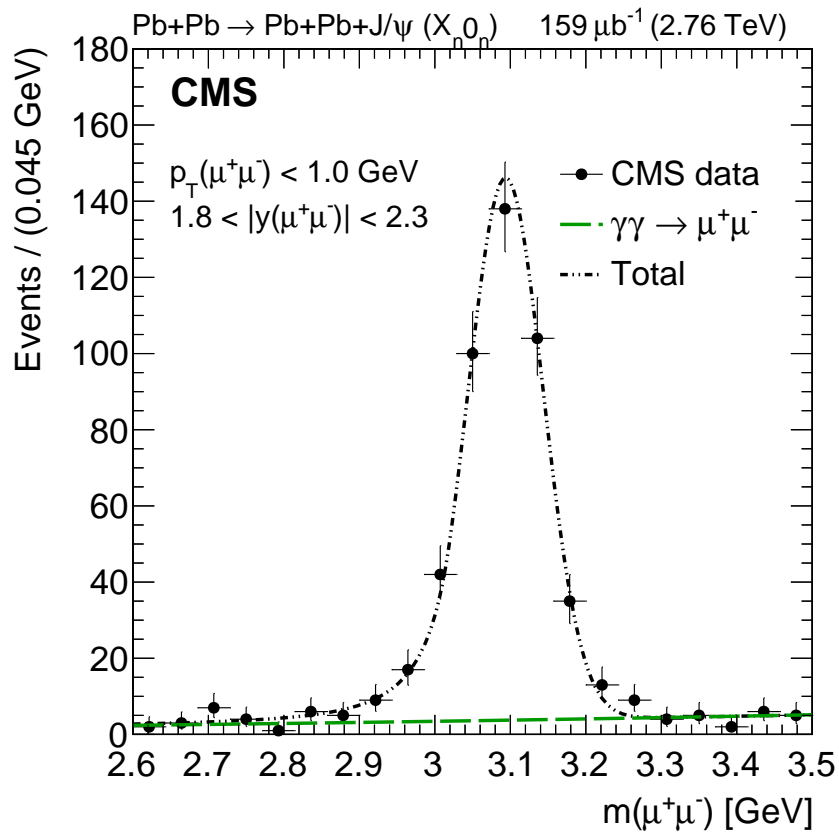


Figure 5.9: The dimuon invariant mass distribution for selected data in the range $2.6 < m(\mu^+\mu^-) < 3.5 \text{ GeV}$ for the break-up mode (X_{n0n}). The green curve is a second-order polynomial and represents the $\gamma + \gamma$ component and the black curve shows the sum of all components ($\gamma + \gamma$, coherent and incoherent J/ψ) [3].

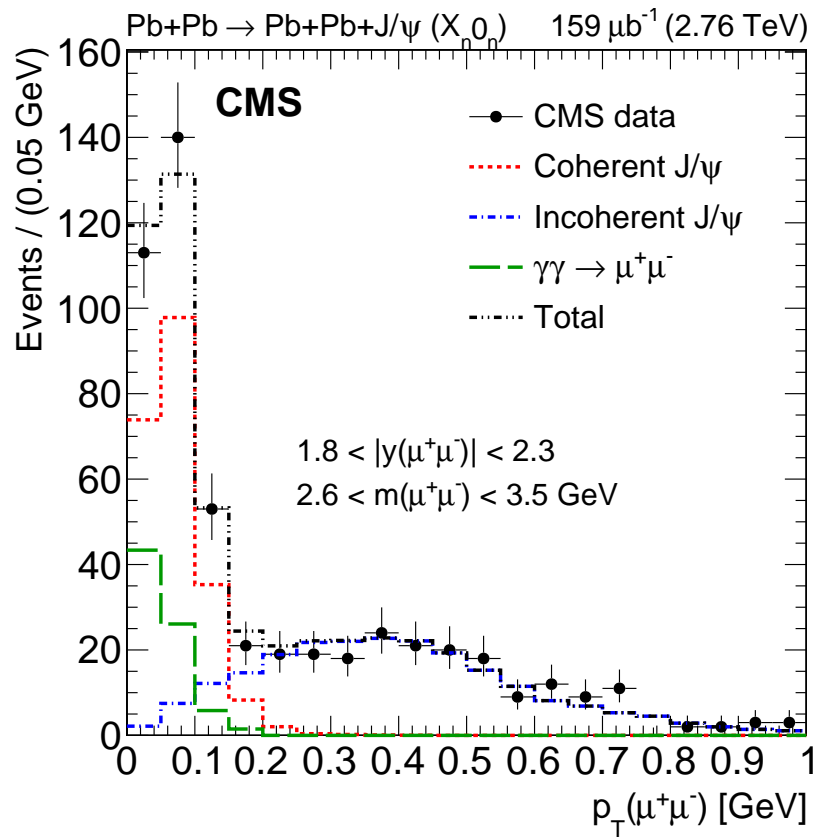


Figure 5.10: The p_T distribution for opposite-sign muon pair with $p_T < 1.0\text{GeV}$ and $1.8 < |y| < 2.3$. The red, blue and green curves represent coherent, incoherent and $\gamma + \gamma$ events separately and the black line shows the sum of all components [3].

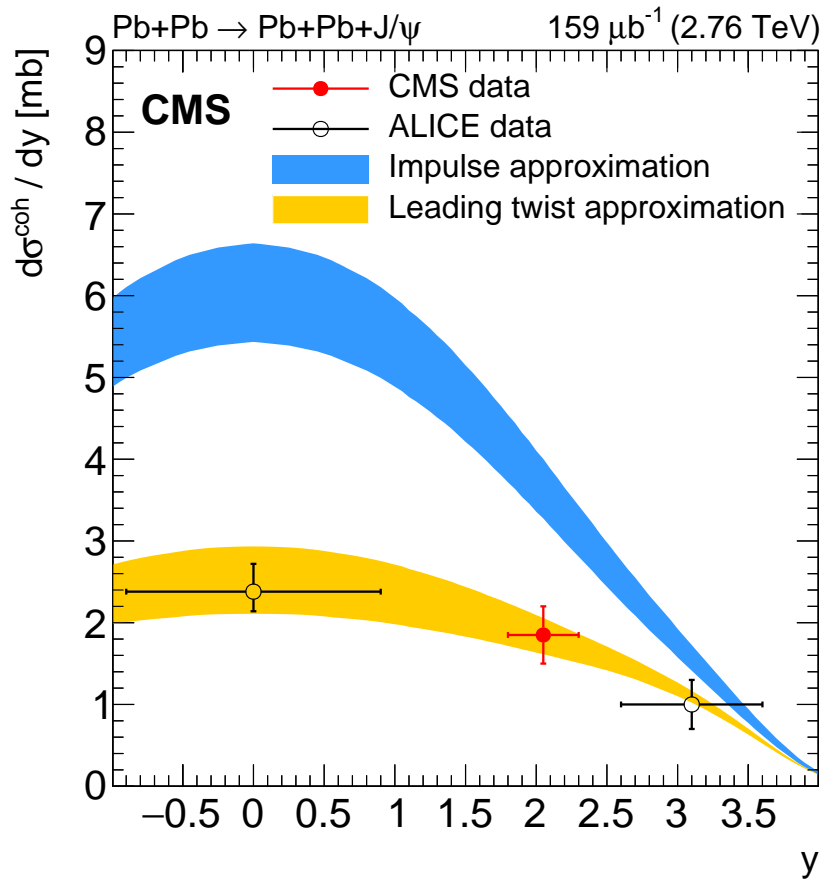


Figure 5.11: Differential cross section in dependence on rapidity for coherently photoproduced J/ ψ measured by CMS and ALICE. The horizontal bars represent the rapidity range of the measurements and the vertical error bars include statistical and systematic uncertainties [3].

Chapter 6

Analysis

In this chapter I present my contribution to the measuring the cross section of coherently photoproduced J/ψ in UPCs at $\sqrt{s_{NN}} = 5.02$ TeV with emission of forward neutrons.

6.1 Data samples

The analysis reported in this chapter is based on data collected in years 2015 and 2018 during Run 2 at the center-of-mass energy $\sqrt{s_{NN}} = 5.02$ TeV by ALICE experiment. In 2018 two run periods were taken 2018q and 2018r, where run period LHC18q corresponds to setup of solenoid with positive polarity and 2018r corresponds to solenoid with negative polarity. Below are listed the runs, which were selected as a good runs for physics analysis by the Data Preparation Group of ALICE.

Good runs selected for period LHC15o - NanoAOD 488 20190613-1350 - muon_calor_pass1:

- 244918, 244980, 244982, 244983, 245064, 245066, 245068, 245145, 245146, 245151, 245152, 245231, 245232, 245233, 245253, 245259, 245343, 245345, 245346, 245347, 245353, 245401, 245407, 245409, 245410, 245446, 245450, 245496, 245501, 245504, 245505, 245507, 245535, 245540, 245542, 245543, 245554, 245683, 245692, 245700, 245705, 245729, 245731, 245738, 245752, 245759, 245766, 245775, 245785, 245793, 245829, 245831, 245833, 245949, 245952, 245954, 245963, 245996, 246001, 246003, 246012, 246036, 246037, 246042, 246048, 246049, 246053, 246087, 246089, 246113, 246115, 246148, 246151, 246152, 246153, 246178, 246181, 246182, 246217, 246220, 246222, 246225, 246272, 246275, 246276, 246390, 246391, 246392, 246424, 246428, 246431, 246433, 246434, 246487, 246488, 246493, 246495, 246675, 246676, 246750, 246751, 246755, 246757, 246758, 246759, 246760, 246763, 246765, 246804, 246805, 246806, 246807, 246808, 246809, 246844, 246845, 246846, 246847, 246851, 246855, 246859, 246864, 246865, 246867, 246871, 246930, 246937, 246942, 246945, 246948, 246949, 246980, 246982, 246984, 246989, 246991, 246994

Good runs selected for period LHC18q - NanoAOD 501 20190723-1440 - muon_calor_pass3:

- 296623, 296622, 296621, 296619, 296618, 296616, 296615, 296594, 296553, 296552, 296551, 296550, 296549, 296548, 296547, 296516, 296514, 296512,

296511, 296510, 296509, 296472, 296433, 296424, 296423, 296420, 296419, 296415, 296414, 296383, 296381, 296380, 296379, 296378, 296377, 296376, 296375, 296360, 296359, 296358, 296357, 296355, 296354, 296353, 296352, 296312, 296309, 296307, 296304, 296303, 296280, 296279, 296275, 296273, 296270, 296269, 296247, 296246, 296244, 296243, 296242, 296241, 296240, 296198, 296197, 296196, 296195, 296194, 296192, 296191, 296143, 296142, 296135, 296134, 296133, 296132, 296128, 296123, 296074, 296068, 296066, 296065, 296063, 296062, 296061, 296060, 296016, 295947, 295945, 295943, 295942, 295941, 295937, 295936, 295916, 295915, 295913, 295910, 295909, 295908, 295881, 295872, 295863, 295861, 295860, 295859, 295856, 295855, 295854, 295853, 295831, 295829, 295826, 295825, 295822, 295819, 295818, 295816, 295791, 295788, 295786, 295763, 295762, 295759, 295758, 295756, 295755, 295754, 295753, 295725, 295723, 295721, 295720, 295719, 295718, 295717, 295716, 295714, 295712, 295677, 295676, 295675, 295673, 295671, 295668, 295667, 295666, 295665, 295615, 295612, 295611, 295610, 295589, 295588, 295587, 295586, 295585, 295584, 295581, 295530, 295494, 295488, 295424, 295274

Good runs selected for period LHC18r - NanoAOD 501 20190723-1441 - muon_calor_pass3:

- 297624, 297623, 297595, 297590, 297589, 297588, 297558, 297557, 297544, 297542, 297541, 297540, 297537, 297512, 297483, 297481, 297479, 297452, 297451, 297450, 297446, 297442, 297441, 297415, 297414, 297413, 297408, 297406, 297405, 297403, 297380, 297379, 297372, 297367, 297366, 297363, 297336, 297335, 297333, 297332, 297331, 297329, 297328, 297326, 297325, 297324, 297323, 297322, 297321, 297319, 297317, 297315, 297312, 297311, 297310, 297278, 297277, 297222, 297221, 297219, 297218, 297196, 297195, 297194, 297193, 297133, 297132, 297129, 297128, 297124, 297123, 297119, 297118, 297117, 297085, 297035, 297031, 297029, 296979, 296977, 296976, 296975, 296971, 296969, 296968, 296967, 296966, 296941, 296938, 296935, 296934, 296932, 296931, 296930, 296903, 296900, 296899, 296894, 296890, 296852, 296851, 296850, 296849, 296848, 296839, 296838, 296836, 296835, 296799, 296794, 296793, 296791, 296790, 296787, 296786, 296785, 296784, 296781, 296752, 296750, 296749, 296694, 296693, 296691, 296690

6.2 The triggers

For this analysis, only UPC events in which dimuon pair is created, but nothing else, are relevant. To select such events CMUP11-B-NOPF-MUFAST trigger was used. The muon trigger used in this analysis for both 2015 and 2018 data has different components and described below: CMUP11-B-NOPF-MUFAST = !0VBA&!0UBA&!0UBC&0MUL, where

- !0VBA - no signal in VOA with beam-beam timing
- !0UBA - no signal in ADA with beam-beam timing
- !0UBC - no signal in ADC with beam-beam timing
- 0MUL - low $-p_T$ unlike sign dimuon trigger

We ask for the events for which there is no signal in V0A, ADA and ADC detector within a beam-beam timing and for which we detect two unlike sign muons over low- p_T in muon spectrometer. The low- p_T trigger threshold was set to 1 GeV/ c .

The integrated luminosity for 2015 data is $216\mu\text{b}^{-1}$ and $538\mu\text{b}^{-1}$ for data from year 2018.

6.3 Selection of events

In this section the conditions of the selecting exactly two unlike sign muons in ultra-peripheral collisions are summarized.

6.3.1 Event selection criteria

The global conditions required on the candidate event, which are selected by mentioned trigger, are as follows:

- No signal in V0A detector
- No signal in V0C detector or maximum two hits with timing corresponding to beam-beam events because the rapidity range of the muon spectrometer is slightly wider than V0C, so then produced muons can miss the V0C but still hit the muon detector.
- Offline veto on ADA and ADC detectors - it improves the quality of the online trigger
- No signal in the SPD because no activity in the central barrel is expected
- Exactly two unlike sign muons detected in the muon spectrometer

6.3.2 Track selection

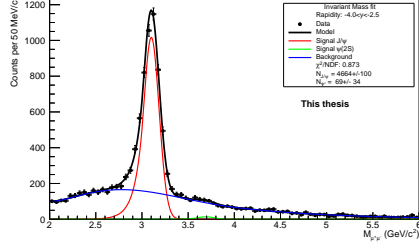
Several requirements on each muon track are applied:

- The pseudorapidity of each track is in range $-4.0 < \eta_\mu < -2.5$, so the muon can be detected by the muon spectrometer
- The radial position of each track at the entrance to the absorber is between $17.5 < R_{abs} < 89.5\text{cm}$ to ensure that the track passes through the absorber's homogeneous region.
- Each muon detected by the muon tracking chamber is matched with the muon detected in the muon trigger chamber.
- Cut applied on momentum multiplied by the distance of closest approach of each track to the interaction point, $p \times DCA$ to reduce beam-induced background.

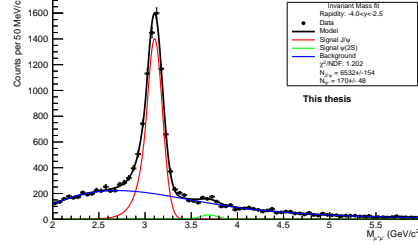
6.3.3 Dimuon selection

In the following the selection condition on each pair of muons are summarized:

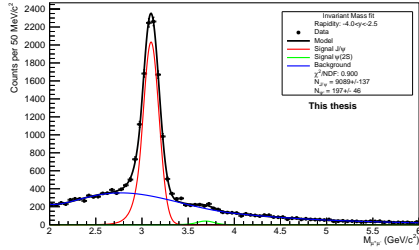
- The opposite electric charge of two muons.



(a) The invariant mass $M_{\mu^+\mu^-}$ in full rapidity range, run period 2015o.



(b) The invariant mass $M_{\mu^+\mu^-}$ in full rapidity range, run period 2018q.



(c) The invariant mass $M_{\mu^+\mu^-}$ in full rapidity range, run period 2018r.

- The dimuon rapidity should be in the interval $-4.0 < y_{\mu\mu} < -2.5$ so that is in the spectrometer rapidity acceptance.
- The transverse momentum of the dimuon is $p_T < 250 \text{ MeV}/c$ to ensure that the muon pair is produced from coherent J/ψ photoproduction.
- The invariant mass of dimuon pair is in the range $2.85 < M_{\mu\mu} < 3.35 \text{ GeV}/c^2$.

6.4 The invariant mass distribution

As a cross check of the results from paper [2] the invariant mass of muon pair is shown in Fig. 6.1a, Fig. 6.1b and Fig. 6.1c separately for the 2015o, 2018q and 2018r periods, respectively. The coherence of the collision was ensured by transverse momentum cut of $p_T < 0.25 \text{ GeV}/c$. The J/ψ and Ψ' peaks were fitted with the CrystalBall function and the background with the exponential function. The total number of coherently produced J/ψ mesons is consistent with the result from the publication [2]. The invariant mass in six rapidity intervals can be seen in 6.1 from run period 2018q.

6.5 Energy spectrum of ZDC

Exclusive photoproduction of J/ψ accompanied by additional forward neutron emission is analyzed by studying the energy deposit in Zero Degree Calorimeter detectors (ZDCs). The average energy deposit in ZDC by a single neutron corresponds to its

energy, which is, in this case, the energy of the beam. The average energy is proportional to the number of absorbed neutrons and the energy distribution is characterized by Gaussian. The mean of the Gaussian is equal to the beam energy $\mu = E_0$ and the dispersion σ_1 depends on E_0 . Therefore, the energy resolution σ_1/μ_1 is also dependent on E_0 . Two functions which are usually considered to evaluate the resolution are mentioned here:

$$\frac{\sigma_1}{\mu_1} = \sqrt{\frac{a^2}{E_0} + b^2}, \quad (6.1)$$

$$\frac{\sigma_1}{\mu_1} = \frac{c}{\sqrt{E_0}} + d, \quad (6.2)$$

These two formulas are nearly identical in the case when the second term is much smaller in comparison to the first one and $a \approx c$. The larger the beam energy is, the better is the resolution. For instance, at $E_0 = 2510$ GeV, (corresponding to $\sqrt{s_{NN}} = 5.02$ TeV), the ALICE neutron ZDC resolution [15] was calculated to be 11.5%, with parameters $a = 2.566 \text{ GeV}^{1/2}$ and $b = 0.103$, using Eq. 6.1.

The number of emitted neutrons is obtained from the fit of the energy spectrum. The fitting function $F(E)$ is sum of four Gaussians $f_i(E)$, where $i = 1, 2, 3, 4$ stands for number of emitted neutrons in each event.

$$F(E) = \sum_{i=1}^4 f_i(E) = \sum_{i=1}^4 \frac{N_i}{\sqrt{2\pi}\sigma_i} e^{-\frac{(E-\mu_i)^2}{2\sigma_i^2}}, \quad (6.3)$$

where N_i is the normalization constant corresponding to the number of events with i neutrons. For mean and dispersion of each peak correspond to $\mu_1 = E_0$, $\mu_i = i\mu_1$ and $\sigma_i = \sqrt{i}\sigma_1$.

However, it is not possible to catch all the forward neutrons. They can be lost due to limited ZDC geometrical acceptance. Some of the neutrons don't hit the calorimeter at all or they deposit only partial energy due to their peripheral impact on the ZDC and shower leakage. Therefore determination of N_i is not straightforward. For instance, in case of an event, when three neutrons were emitted, one or two neutrons can be lost. Then these events are misidentified as one or two neutron events. So in Eq. 6.3, number of detected events n_i is used instead of real N_i .

For UPC Pb–Pb collisions at $\sqrt{s_{NN}} = 5.02$ TeV the energy spectrum was calculated using the Eq. 6.1 and Eq. 6.3. The resolution $\frac{\sigma_1}{\mu_1} = 0.15$ and it is shown in Fig. 6.2.

To calculate the cross section of J/ψ with neutron emission (different neutron channels) some corrections are needed. Such as the acceptance correction to ZDC energy spectra mentioned above, corrections corresponding to efficiency of the ZDC and the pile-up consideration. All these corrections are not considered in this work.

The selection of events with signal in ZNA and ZNC is performed using the timing information. The time information is provided by the a Time to Digital Converter (TDC). Applying a cut on timing information ($-2 \text{ ns} < t < 2 \text{ ns}$), the small contribution from collisions between main and satellite bunches are rejected. In Fig. 6.3 the timing information of ZNA and ZNC is shown after the cut. One can notice that there is much higher activity in the ZNC detector than in the ZNA. The energy distributions for events that satisfied the timing cut can be found on Fig. 6.4 for periods 2015o and 2018q. One can see that there is a signal around zero in both ZNA and ZNC detectors for period 2015o. The reason of this fact is not clear to me but these events need to be cut off for the further analysis. However, the cut off is not applied in this work and it is planned for the future. For both displayed periods we can nicely see the peak of one detected neutron around $2500 \text{ GeV}/c^2$.

For the data 2018q I used the Gaussians to fit the first two peaks corresponding to one and two neutron events, see Fig. 6.5. The fits did not come up very well and it needs to be work on.

6.6 Transverse momentum distribution

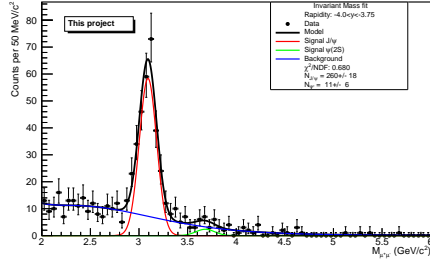
The reactions with neutron emission are studied by looking at the energy spectrum of the ZDC detectors, which was shown above. I used neutron channel listed below:

- (0n0n)-empty ZDC detector on both sides
- (XnXn)-one or more neutrons detected in both sides of ZDC detector
- (0nXn)-empty ZNA and at least one neutron in ZNC
- (Xn0n)-at least one neutron in ZNA and none in ZNC

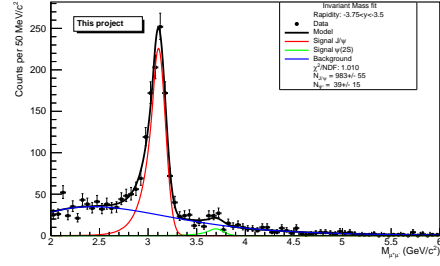
The transverse momentum for different neutron channels were studied. I did not used any cut on p_T to see if there are some differences in the background. The p_T distribution are shown in Fig. 6.6 for the 2018r period. We can notice that for the case, when there is a signal in ZNC detector while ZNA is empty the p_T distribution looks very different, so the background is different. The highest number of events is for the case of no neutron emission during the collision. The case, when neutron was emitted in the direction of the produced J/ψ , detected in ZNC, follows.

6.7 Rapidity distribution

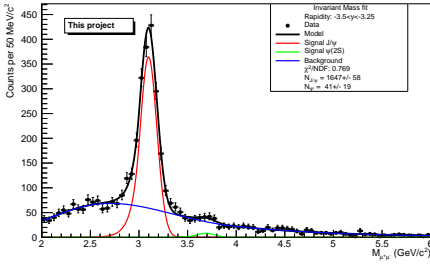
The rapidity distributions for each neutron channel is displayed Fig. 6.7 and we can see that the shape of the distributions is very similar for different neutron channels. It is planned to look at the p_T distributions in several rapidity bins however, there is so few events in some channels.



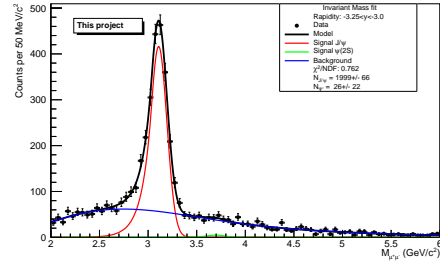
(a) Rapidity range $-4.0 < y < -3.75$



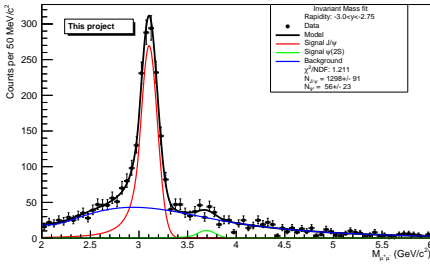
(b) Rapidity range $-3.75 < y < -3.5$



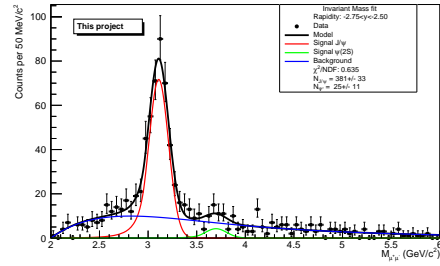
(c) Rapidity range $-3.5 < y < -3.25$



(d) Rapidity range $-3.25 < y < -3.0$



(e) Rapidity range $-3.0 < y < -2.75$



(f) Rapidity range $-2.75 < y < -2.5$

Figure 6.1: The mass spectrum of dimuon pair for different rapidity intervals.

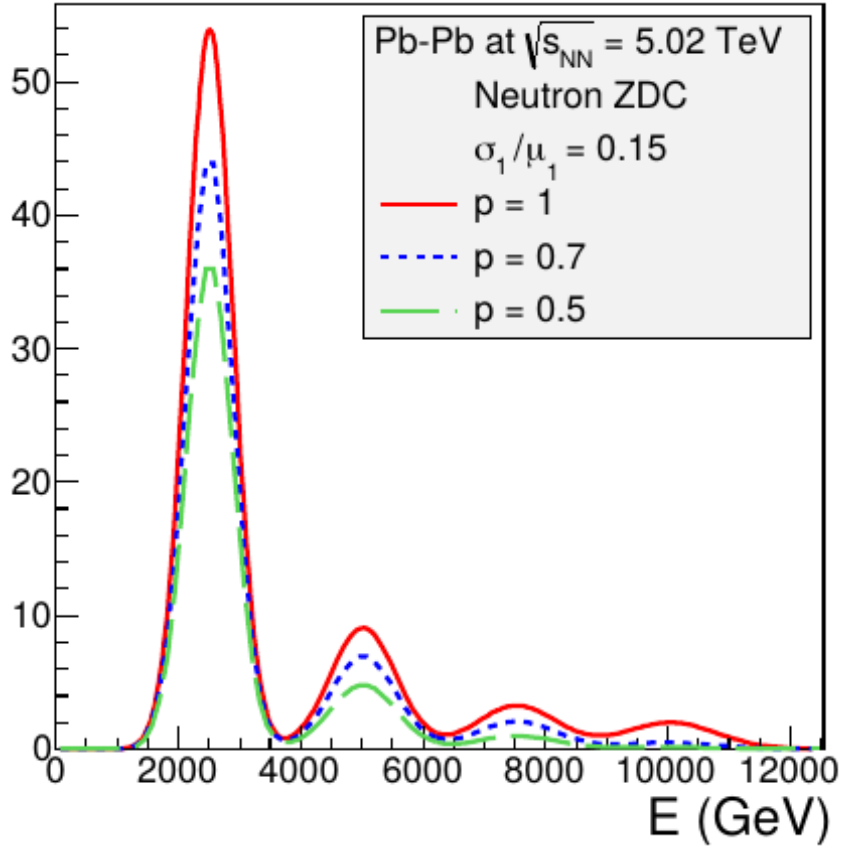
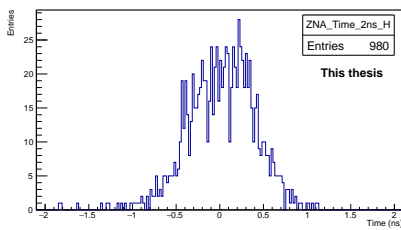
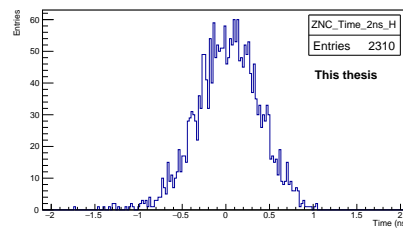


Figure 6.2: Model of energy distribution (arb. unit) in neutron ZDC in UPC Pb-Pb collisions at $\sqrt{s_{NN}} = 5.02$ TeV [15].

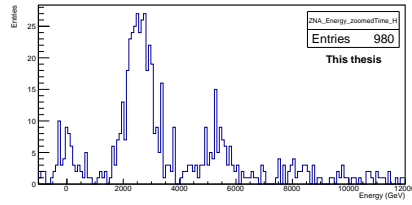


(a) ZNA detector

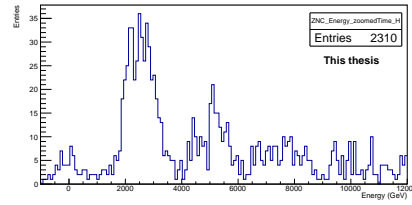


(b) ZNC detector

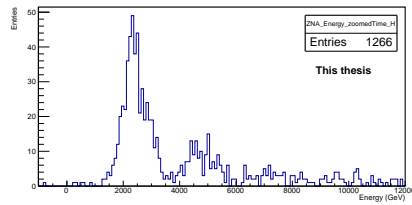
Figure 6.3: Timing information of ZNA and ZNC detectors within the range $-2.0 < t < 2.0$ ns for 2015 data.



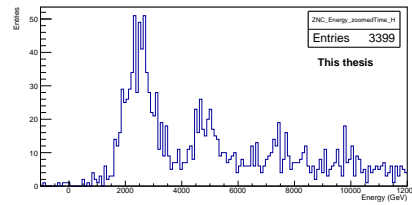
(a) Energy deposited in ZNA detector, 2015o data.



(b) Energy deposited in ZNC detector, 2015o data.

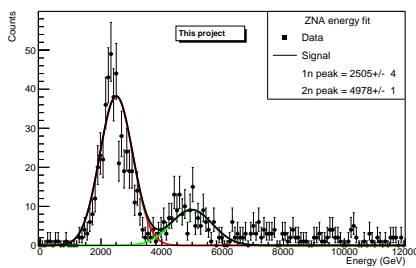


(c) Energy deposited in ZNC detector, 2018q data.

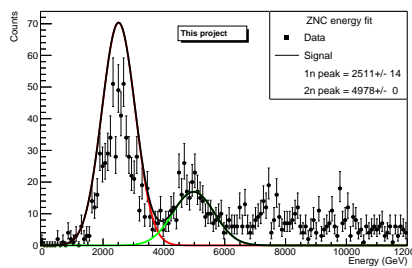


(d) Energy deposited in ZNC detector, 2018q data.

Figure 6.4: ZNA and ZNC energy spectrum for events within $-2.0 < t < 2.0$ ns timing. The peaks correspond to neutron emission of $1n, 2n, 3n, 4n$.

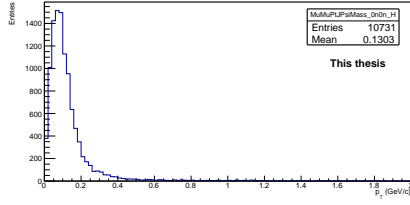


(a) Energy deposited in ZNA detector.

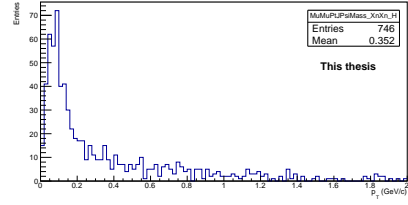


(b) Energy deposited in ZNC detector.

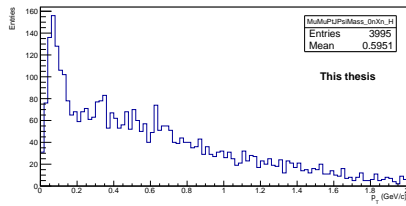
Figure 6.5: ZNA (a) and ZNC (b) energy spectrum for events within $-2.0 < t < 2.0$ ns timing. The peaks correspond to neutron emission of $1n, 2n, \dots$ and are fitted by the Gaussian. Data period 2018q.



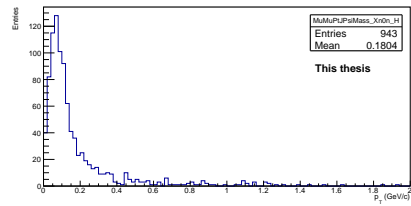
(a) (0n0n)



(b) (XnXn)

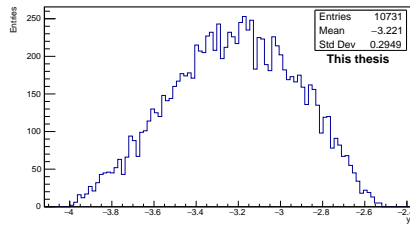


(c) (0nXn)

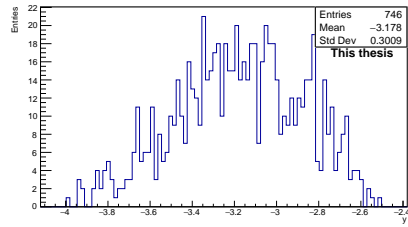


(d) (Xn0n)

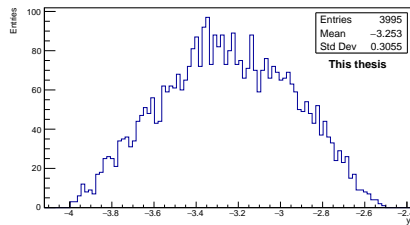
Figure 6.6: The transverse momentum distribution for events which satisfy ZDC selection for different neutron channels, run period 2018r.



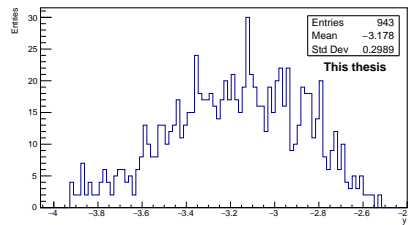
(a) (0n0n)



(b) (XnXn)



(c) (0nXn)



(d) (Xn0n)

Figure 6.7: The transverse momentum distribution for events which satisfy ZDC selection for different neutron channels, run period 2018r.

Chapter 7

Summary

In the Chapter 2 I summarized our view of nucleon and nucleus structure nowadays. I introduced the phenomena which are recent topics of our interests, such saturation and gluon nuclear shadowing in low- x region.

The next Chapter 3 was dedicated to the description of coherent J/ψ photoproduction in Ultra-peripheral collisions as a tool to study the nucleon structure in values of low- x . The cross section of such measurements was described and a theoretical model predicting the cross section of vector meson photoproduction was presented.

The ALICE detector was described in the Chapter 4. The emphasis is put on the subdetectors which are important for this measurement, such as Muon Spectrometer and Zero Degree Calorimeter.

Publications that presented the measurements of J/ψ photoproduction were summarized in Chapter 5. Two ALICE papers and one paper from CMS collaboration were presented.

In Chapter 6 my contribution to the analysis of coherent J/ψ photoproduction measured by ALICE in forward rapidity range in Pb-Pb ultra-peripheral collisions at center-of-mass energy $\sqrt{s_{NN}} = 5.02$ TeV during Run 2 in periods 2015o, 2018q and 2018r is presented. The cross check of some published results by producing the invariant mass of dimuon pair was done for each period separately and the number of coherently photoproduced J/ψ mesons is consistent with the results. The events with the additional forward neutrons were studied, the p_T distribution for different neutron channels was studied. It was shown that for different neutron channels we detect different number of events, and background is also various. It is believed that we will be able to decouple two terms contributing to the cross section of the J/ψ photoproduction in Pb-Pb UPCs and investigate the structure of nucleons and nuclei in even lower x region, ($x \sim 10^{-5}$).

In the future I plan to work on my contribution to the analysis of coherently photoproduced J/ψ accompanied by a forward neutron emission to separate two contributions to the cross section.

Bibliography

- [1] **ALICE** Collaboration, B. Abelev et al., *Coherent J/ψ photoproduction in ultra-peripheral Pb-Pb collisions at $\sqrt{s_{NN}} = 2.76$ TeV*, *Phys. Lett.* **B718** (2013) 1273–1283, [arXiv:1209.3715].
- [2] **ALICE** Collaboration, S. Acharya et al., *Coherent J/ψ photoproduction at forward rapidity in ultra-peripheral Pb-Pb collisions at $\sqrt{s_{NN}} = 5.02$ TeV*, arXiv:1904.06272.
- [3] **CMS** Collaboration, V. Khachatryan et al., *Coherent J/ψ photoproduction in ultra-peripheral PbPb collisions at $\sqrt{s_{NN}} = 2.76$ TeV with the CMS experiment*, *Phys. Lett.* **B772** (2017) 489–511, [arXiv:1605.06966].
- [4] R. W. Mcallister and R. Hofstadter, *Elastic Scattering of 188-MeV Electrons From the Proton and the α Particle*, *Phys. Rev.* **102** (1956) 851–856.
- [5] F. Halzen and A. D. Martin, *QUARKS AND LEPTONS: AN INTRODUCTORY COURSE IN MODERN PARTICLE PHYSICS*. 1984.
- [6] J.-P. Blaizot, *High gluon densities in heavy ion collisions*, *Rept. Prog. Phys.* **80** (2017), no. 3 032301, [arXiv:1607.04448].
- [7] N. Armesto, *Nuclear shadowing*, *J. Phys.* **G32** (2006) R367–R394, [hep-ph/0604108].
- [8] A. J. Baltz, *The Physics of Ultrapерipheral Collisions at the LHC*, *Phys. Rept.* **458** (2008) 1–171, [arXiv:0706.3356].
- [9] V. Guzey, E. Kryshen, and M. Zhalov, *Coherent photoproduction of vector mesons in ultraperipheral heavy ion collisions: Update for run 2 at the CERN Large Hadron Collider*, *Phys. Rev.* **C93** (2016), no. 5 055206, [arXiv:1602.01456].
- [10] G. Herrera Corral, *Diffractive Physics with ALICE at the LHC: the control of quantum collisions*, *J. Phys. Conf. Ser.* **624** (2015), no. 1 012008.
- [11] G. Contin, *Performance of the present ALICE Inner Tracking System and studies for the upgrade*, *JINST* **7** (2012) C06007.
- [12] **ALICE** Collaboration, G. Martinez, *The Muon spectrometer of the ALICE experiment*, *Nucl. Phys.* **A749** (2005) 313–319, [hep-ex/0410061].
- [13] D. Stocco, *Development of the ALICE Muon Spectrometer: Preparation for data taking and heavy flavor measurement*. PhD thesis, Turin U., 2008.

- [14] R. Arnaldi, E. Chiavassa, C. Cical, P. Cortese, A. Falco, G. Dellacasa, N. Marco, A. Ferretti, M. Gallio, P. Macciotta, A. Masoni, A. Musso, C. Oppedisano, A. Piccotti, G. Puddu, E. Scalas, E. Scomparin, S. Serci, E. Siddi, C. Soave, G. Usai, and E. Vercellin, *Performances of zero degree calorimeters for the alice experiment*, *Nuclear Instruments and Methods in Physics Research Section A: Accelerators, Spectrometers, Detectors and Associated Equipment* **456** (2001), no. 3 248 – 258.
- [15] U. Dmitrieva and I. Pshenichnov, *On the performance of Zero Degree Calorimeters in detecting multinucleon events*, *Nucl. Instrum. Meth.* **A906** (2018) 114–119, [arXiv:1805.01792].
- [16] A. De Roeck and R. S. Thorne, *Structure Functions*, *Prog. Part. Nucl. Phys.* **66** (2011) 727–781, [arXiv:1103.0555].
- [17] M. G. Ryskin, *Diffraction J/ψ electroproduction in LLA QCD*, *Z. Phys.* **C57** (1993) 89–92.
- [18] V. Guzey, M. Strikman, and M. Zhalov, *Disentangling coherent and incoherent quasielastic J/ψ photoproduction on nuclei by neutron tagging in ultraperipheral ion collisions at the LHC*, *Eur. Phys. J.* **C74** (2014), no. 7 2942, [arXiv:1312.6486].
- [19] T.-M. Yan and S. D. Drell, *The Parton Model and its Applications*, *Int. J. Mod. Phys.* **A29** (2014) 0071, [arXiv:1409.0051].
- [20] B. Kopeliovich and B. Povh, *Nuclear shadowing and the proton structure function at small x* , hep-ph/9504380.
- [21] M. Kliemant, R. Sahoo, T. Schuster, and R. Stock, *Global Properties of Nucleus-Nucleus Collisions*, *Lect. Notes Phys.* **785** (2010) 23–103, [arXiv:0809.2482].
- [22] J. G. Contreras and J. D. Tapia Takaki, *Ultra-peripheral heavy-ion collisions at the lhc*, *International Journal of Modern Physics A* **30** (2015), no. 08 1542012, [https://doi.org/10.1142/S0217751X15420129].
- [23] V. Guzey and M. Zhalov, *Exclusive J/ψ production in ultraperipheral collisions at the LHC: constrains on the gluon distributions in the proton and nuclei*, *JHEP* **10** (2013) 207, [arXiv:1307.4526].
- [24] **ALICE** Collaboration, B. Abelev et al., *Measurement of the cross section for electromagnetic dissociation with neutron emission in pb-pb collisions at $\sqrt{s_{NN}}=2.76$ TeV*, *Phys. Rev. Lett.* **109** (Dec, 2012) 252302.
- [25] A. J. Baltz, S. R. Klein, and J. Nystrand, *Coherent vector meson photoproduction with nuclear breakup in relativistic heavy ion collisions*, *Phys. Rev. Lett.* **89** (2002) 012301, [nucl-th/0205031].
- [26] **ALICE** Collaboration, K. Aamodt et al., *The ALICE experiment at the CERN LHC*, *JINST* **3** (2008) S08002.
- [27] V. Fílová, *Coherent production $j/\psi \rightarrow p\bar{p}$ in pb-pb ultra-peripheral collisions*, *Bachelor's thesis*, 2016. https://physics.fjfi.cvut.cz/publications/ejcf/bp_ejcf_16_filova.pdf, Last accessed on 2019-09-09.

- [28] **ALICE** Collaboration, E. Abbas et al., *Performance of the ALICE VZERO system*, *JINST* **8** (2013) P10016, [arXiv:1306.3130].
- [29] S. R. Klein, J. Nystrand, J. Seger, Y. Gorbunov, and J. Butterworth, *STARlight: A Monte Carlo simulation program for ultra-peripheral collisions of relativistic ions*, *Comput. Phys. Commun.* **212** (2017) 258–268, [arXiv:1607.03838].
- [30] **ALICE** Collaboration, B. B. Abelev et al., *Exclusive J/ψ photoproduction off protons in ultra-peripheral p-Pb collisions at $\sqrt{s_{NN}} = 5.02$ TeV*, *Phys. Rev. Lett.* **113** (2014), no. 23 232504, [arXiv:1406.7819].
- [31] V. Guzey, M. Strikman, and M. Zhalov, *Disentangling coherent and incoherent quasielastic J/ψ photoproduction on nuclei by neutron tagging in ultraperipheral ion collisions at the LHC*, *The European Physical Journal C* **74** (Jul, 2014) 2942.